Mon. Not. R. Astron. Soc. **000**, 000–000 (0000) Printed 5 October 2018 (MN LATEX style file v2.2)

Hubble Space Telescope spectra of the type Ia supernova SN 2011fe: A low-energy delayed detonation of a white dwarf with $Z < Z_{\odot}$.

P. A. Mazzali[1,2,3] ⋆, M. Sullivan[4], S. Hachinger[2,5], R. S. Ellis[6], P. E. Nugent[7], D. A. Howell[8,9], A. Gal-Yam[10], K. Maguire[11], J. Cooke[12], R. Thomas[6]

[1]*Astrophysics Research Institute, Liverpool John Moores University, Twelve Quays House, Egerton Wharf, Birkenhead, Wirral, CH41 1LD, UK*
[2]*Istituto Nazionale di Astrofisica-OAPd, vicolo dell'Osservatorio 5, 35122 Padova, Italy*
[3]*Max-Planck-Institut für Astrophysik, Karl-Schwarzschild-Str. 1, D-85748 Garching, Germany*
[4]*School of Physics and Astronomy, University of Southampton, Southampton, SO17 1BJ, UK*
[5]*Institut für Theoretische Physik und Astrophysik, Universität Würzburg, Emil-Fischer-Str. 31, 97074 Würzburg, Germany*
[6]*Cahill Center for Astrophysics, California Institute of Technology, Pasadena, CA 91125, USA*
[7]*Computational Cosmology Center, Lawrence Berkeley National Laboratory, 1 Cyclotron Rd., Berkeley CA 94720, USA*
[8]*Las Cumbres Observatory Global Telescope Network, Goleta, CA 93117, USA*
[9]*Department of Physics, University of California, Santa Barbara, CA 93106-9530, USA*
[10]*Benoziyo Center for Astrophysics, Weizmann Institute of Science, 76100 Rehovot, Israel*
[11]*Department of Physics (Astrophysics), University of Oxford, Keble Road, Oxford OX1 3RH*
[12]*Centre for Astrophysics & Supercomputing, Swinburne University of Technology, Mail H30, PO Box 218, Hawthorn, Victoria 3122, Australia*

5 October 2018

ABSTRACT

Hubble Space Telescope spectroscopic observations of the nearby type Ia supernova (SN Ia) SN 2011fe, taken on 10 epochs from -13.5 to $+41$ days relative to B-band maximum light, and spanning the far-ultraviolet (UV) to the near-infrared (IR) are presented. This spectroscopic coverage makes SN 2011fe the best-studied local SN Ia to date. SN 2011fe is a typical moderately-luminous SN Ia with no evidence for dust extinction. Its near-UV spectral properties are representative of a larger sample of local events studied in Maguire et al. (2012). As a result, conclusions inferred from our detailed investigations are likely representative of those for other normal SNe Ia. The near-UV to optical spectra of SN 2011fe are modelled with a Monte Carlo radiative transfer code using the technique of 'abundance tomography', providing tight constraints on the density structure and abundance stratification of the event. SN 2011fe was a relatively weak explosion, with moderate Fe-group yields. Although its density structure is close to the 'standard' SN Ia pure deflagration explosion model W7, an improved model was developed which demonstrates that the ejecta of SN 2011fe have a more pronounced high-velocity tail, typical of a detonation wave affecting the outer layers. This improved model has a lower energy than typical delayed-detonation models. The derived Fe abundance in the outermost layer is consistent with the metallicity $\sim 0.5 Z_{\odot}$ at the SN explosion site in M101. Importantly, the spectroscopic rise time of ~ 19 days is significantly longer than that measured from the early optical light curve, implying a 'dark phase of ~ 1 day. Such an extension in the rise time has significant implications when deducing the properties of the white dwarf and binary system from the early photometric behaviour.

Key words: supernovae: general – supernovae: individual (SN 2011fe) – techniques: spectroscopic – radiative transfer

1 INTRODUCTION

Type Ia supernovae (SNe Ia) remain a well-exploited cosmological probe and an immediate route to understanding the nature of dark energy (e.g. Riess et al. 1998; Perlmutter et al. 1999; Riess et al. 2007; Kessler et al. 2009; Sullivan et al. 2011; Suzuki et al. 2012). However, the exact nature of the progenitor system is still not well understood, with various astrophysical systematics potentially affecting cosmological measurements (for summaries, see Conley et al. 2011; Howell 2011; Astier 2012). A particularly important systematic is the role of the metallicity, or composition, of

⋆ E-mail: P.Mazzali@ljmu.ac.uk

the exploding white dwarf star on the outcome of the explosion and the properties of SNe Ia.

It has long been known that the ultraviolet (UV) region of SN Ia spectra effectively traces compositional or metallicity effects (Hoeflich et al. 1998; Lentz et al. 2000). Although the physics underlying the formation of SN Ia UV spectra is complex, the UV is probably the best diagnostic of iron-group element abundances in the outer layers of the SN ejecta (Mazzali 2000; Walker et al. 2012; Hachinger et al. 2013) which are transparent to optical photons. This is closely connected to the density profile of the SN ejecta, and hence to the SN explosion model – the iron-group content of incompletely burned zones is one of the main differences between SN Ia explosions at different metallicity (Iwamoto et al. 1999).

However, data in the UV were historically difficult to obtain. Space observatories are required to perform the observations, and the intrinsic faintness of SNe Ia below ∼2700Å requires targets to be relatively nearby to obtain a useful signal-to-noise (S/N). The *International Ultraviolet Explorer* (*IUE*) and the *Hubble Space Telescope* (*HST*) have both been used (Branch & Venkatakrishna 1986; Jeffery et al. 1992; Kirshner et al. 1993; Cappellaro et al. 1995; Sauer et al. 2008a), but generally the data suffer from poor S/N, with only one well-observed SN Ia near maximum light (SN 1992A; Kirshner et al. 1993) and only a few events with early pre-maximum light coverage (e.g. SN 1990N; Leibundgut et al. 1991). A full compilation of observations up to 2004 can be found in Foley et al. (2008b). More recently, the Advanced Camera for Surveys on *HST* observed four SNe Ia (Wang et al. 2012), but the spectral resolution was low making a detailed study difficult.

Some of these earlier difficulties have been alleviated in modern SN searches, which can provide a significant number of early SN Ia events. The Lick Observatory Supernova Search early discovery of SN 2009ig (Foley et al. 2012c) allowed a reasonably high-S/N UV spectral time series to be obtained using *Swift*, and the fast response of that satellite has also allowed spectral series of several other events, although the S/N below 2700Å is not high (Bufano et al. 2009). *HST*, with its larger aperture, has obtained more spectra with a higher S/N, including high-S/N observations of the relatively fast-declining SN 2011iv (Foley et al. 2012b), although these did not commence until maximum light.

A different approach is to focus on the near-UV region down to $\simeq$ 2900 Å, which is more easily accessible. At high redshift this wavelength range is redshifted into the optical (e.g. Ellis et al. 2008), and a significant sample of single maximum-light near-UV spectra is now available (Ellis et al. 2008; Foley et al. 2008a; Balland et al. 2009; Foley et al. 2012a). In *HST* cycle 17, we successfully obtained single-epoch near-UV spectra of ∼30 lower redshift ($z < 0.08$) SNe Ia at phases close to maximum light (Maguire et al. 2012, hereafter M12), for the most part using early discoveries from the Palomar Transient Factory (PTF; Rau et al. 2009; Law et al. 2009).

M12 presented evidence for evolution in the mean near-UV continuum between $z = 0$ and $z \sim 0.5$, the latter using spectra from Ellis et al. (2008). They demonstrated an excess near-UV flux at ~ 0.5 compared to $z = 0$ at $\simeq 3\sigma$, and showed that this was qualitatively consistent with expected evolutionary effects due to changes in metallicity via a comparison to SN Ia models (Walker et al. 2012). Even stronger near-UV spectral evolution in the same sense as M12 was presented by Foley et al. (2012a), but over a narrower range in redshift, comparing a ground-based $z \simeq 0$ spectrum and a mean spectrum at $z \sim 0.2$. This would then imply a puzzlingly inconsistent evolution between $z = 0.2$ and $z = 0.5$ – although Foley et al. (2012a) caution that selection effects in the $z \sim 0.2$ sample may play a role in this discrepancy.

In cycle 18, we extended the M12 programme to obtain multi-epoch *HST* SN Ia spectra of four events, from the earliest possible epoch to post-maximum light. Our first spectral series, of SN 2010jn, and its detailed analysis using a radiative transfer code are published in Hachinger et al. (2013). SN 2010jn was an energetic SN Ia explosion, with high expansion velocities and significant amounts of iron-group elements in the outer layers of the ejecta, leading to a high opacity consistent with its slow light curve evolution. Interestingly, the detailed spectral modelling of this event implied a 'rise-time' (the time from SN explosion to maximum light in the B-band) longer than that measured from the optical light curve by $\sim$ 1 day. This suggests the existence of a 'dark phase' between the SN explosion and the emergence of the first photons (Piro & Nakar 2013a,b), in turn implying that the bulk of the radioactive heating from ^{56}Ni, which powers the light curve, must lie deep in the ejecta.

In this paper we present *HST* observations of the second event in our cycle 18 programme, the nearby SN Ia SN 2011fe (Nugent et al. 2011), located in M101. Thanks to the proximity of M101 ($\simeq$ 6.4 Mpc, $\mu = 29.04 \pm 0.19$; Shappee & Stanek 2011), SN 2011fe was the brightest SN Ia in the night sky in the 'CCD era', and a comprehensive monitoring campaign carried out across a broad range of wavelengths will make it the best-ever studied SN Ia. Our *HST* data range from the far-UV to the near-infrared (IR), beginning just 4 days after detection and covering 10 epochs. We supplement these *HST* data with spectra taken as part of the PTF follow-up campaign (Parrent et al. 2012). We use a well-established Monte Carlo code (e.g., Lucy 1999; Mazzali 2000; Sauer et al. 2008b; Hachinger et al. 2013) to model this time series of UV/optical spectra. Starting from the outermost regions, we infer the abundance stratification of SN 2011fe, developing a density profile that yields a good fit to the spectra from the UV to the near infrared (IR). We also determine the rise time of the SN from the modelling to compare with the very early SN photometry.

An outline of the paper is as follows. In Section 2 we describe the *HST* observations and their data reduction, and discuss SN 2011fe in the context of other SNe Ia in Section 3. We then introduce the methods used to model the spectra in Section 4, and present the models themselves in Section 5 together with our rise time measurement. We compute spectra for two standard explosion models and a new, hybrid model which yields improved fits to the SN 2011fe spectra. The implications of our results are discussed in Section 6 and we conclude in Section 7.

2 OBSERVATIONS

SN 2011fe was discovered on 2011 August 24.167 (UT) by the PTF using the Palomar 48-in telescope (P48) in M101, at a magnitude of $g \simeq 17.4$ (Nugent et al. 2011, hereafter N11). Within a few hours of discovery, the SN was confirmed as a very early SN Ia using robotic observations with FRODOSPEC on the Liverpool Telescope (LT; Steele et al. 2004). UV/optical/IR spectroscopic observations were subsequently obtained on 10 epochs with the *Hubble Space Telescope (HST)* using the Space Telescope Imaging Spectrograph (STIS), as part of the cycle 18 program #12298: 'Towards a Physical Understanding of the Diversity of Type Ia Supernovae' (PI: Ellis). The phase 2 was submitted in two parts: on 2011 August 25 for the the first few epochs, and on 2011 August 29 for the epochs from maximum light onwards. The later epochs also

included parallel observations with the Wide Field Camera 3 to observe Cepheid variable stars in M101.

In this section, we describe these *HST* observations and their reduction, and detail the construction of a single spectrum on each *HST* epoch. One of these spectra has already been shown in Foley & Kirshner (2013).

2.1 *HST* spectral observations

We used five different STIS configurations using both the CCD and the UV MAMA detectors, covering 4 different wavelength ranges. On all epochs, the near-UV was covered using either NUV-MAMA/230L (giving useful coverage from $\lambda \simeq 1750$ to $\simeq 3150$Å) or CCD/230LB ($\lambda \simeq 1900$ to $\simeq 3050$Å), the optical using CCD/430L ($\lambda \simeq 2950$ to $\simeq 5700$Å), and the near-IR using CCD/750L ($\lambda \simeq 5300$Å to $\simeq 1\mu$m). On one further epoch near maximum light an additional configuration was used to examine the far-UV (FUV-MAMA/140L $\lambda \simeq 1300$ to $\simeq 1700$Å). When using the CCD, we split the observations to assist with cosmic ray rejection ('CR-SPLIT'), and took separate flat-fields after the CCD/750L observations to assist with fringe removal. We used the $0.2''$ slit throughout. A full log of our *HST* observations can be found in Table 1.

At the time of triggering the *HST* ToO, the eventual photometric evolution of SN 2011fe, including its peak brightness and light curve width, was quite uncertain. We thus opted to use the CCD/230LB for the near maximum-light epochs in preference to NUV-MAMA/230L to avoid any possibility of exceeding the MAMA bright-object limits, even though the NUV-MAMA/230L was preferred scientifically because of its superior far-UV coverage. Exposure times, dithers and CR-SPLITs were chosen in an attempt to avoid saturation of this bright target while still efficiently filling the time available in each orbit. For the most part this was successful, although some observations were slightly saturated at the peaks of the SN spectral features because of an under-estimate of the target's eventual brightness and photometric evolution. We discuss the treatment of these saturated spectra in the next section.

2.2 Data reduction

The reduction of the *HST* data followed standard procedures. The data were downloaded from the *HST* archive using the on-the-fly reprocessing (OTFR) pipeline to provide the appropriate 'best' calibration files. As some aspects of the reduction needed to be performed 'by hand' (e.g. fringe removal in the IR data), we used a local CALSTIS installation in IRAF[1] to perform the reductions.

CALSTIS gives fully calibrated and extracted 1-D spectra, where the reduction and extraction is optimised for point sources. It performs initial 2-D image reduction such as image trimming, bias and dark current subtraction, cosmic-ray rejection (using a CR-SPLIT), and flat-fielding. It then performs 1-D spectral extraction, followed by wavelength and flux calibrations. In addition to these standard procedures, we performed three additional steps.

The first step was the fringe frame removal for CCD/750L observations, matching fringes in the CCD/750L fringe flat-field taken with the science observations, to those in the science observations themselves. This generally proceeded satisfactorily, except for the 2011 September 13 epoch where the SN trace was offset from its standard position to allow a different set of Cepheids to be observed in the parallel observations. Unfortunately the fringe-flat position was not updated to reflect this, hence this epoch has less *HST* near-IR coverage and a ground-based Gemini IR spectrum is used in its place (Hsiao et al. 2013).

The second step was the removal of hot pixels, bad pixels, and residual cosmic rays in the data. These were identified by hand by examining the post CR-SPLIT 2-D spectral images. These image defects were then interpolated over in the dispersion direction.

The final additional step was the fixing of the saturation in some of our optical (CCD/430L and CCD/750L) data at the peaks of the SN spectral features (see Table 1). As a point source, the SN has a spatial profile of ~ 11 pixels on the CCD, which is very well aligned with the CCD rows. Where present, saturation affected only the central row of this profile. We corrected for the saturation by taking the flux ratio of the central row to four other rows in the profile (two rows above and two rows below the saturated row) at every wavelength pixel. We then fitted a polynomial function to each of these four flux ratios as a function of wavelength pixel, using only the unsaturated regions in the fit. These polynomial fits can then be interpolated across wavelength pixel regions (columns) that have saturated data, and the SN flux in the saturated central row of the profile inferred from the interpolated flux ratios. The final SN flux in the saturated row is then the weighted mean of these four values, with an error reflecting the variance in these predictions. By testing this procedure on unsaturated regions of the SN spectral profile, and comparing the interpolated flux to the actual observed one, we find an excellent level of agreement.

2.3 Combined spectra

The *HST* spectra were extracted using the standard CALSTIS 1-D spectral extraction tasks, and combined with near-IR data from Hsiao et al. (2013) where available to form a single contiguous spectrum on each epoch. Where the *HST* observations were taken at more than one dither position in a given configuration, we extract each dither position separately and then combine the 1-D spectra. This is in preference to combining the 2-D images directly, as that process is sensitive to the exact sub-pixel centering of the spatial profile on a given row. The individual exposures were rebinned to a common wavelength scale in each wavelength region: 1.6Å over 1000–2900Å (1.4Å when using the CCD/230LB), 2.8Å over 2900–5000Å, 4.9Å over 5000Å–1.1μm, and 7Å over 1.1-2.5μm. The spectra were then optimally combined, weighting by the flux errors in each input pixel.

We used overlapping regions between the spectra to ensure that the flux calibration was consistent, adopting the CCD/430L spectrum as the flux reference at each epoch. Typically, this was a 1–2 per cent correction, although for the 2011-09-13 epoch there was no useful overlap between the FUV-MAMA/140L and the CCD/230LB data, so we did not adjust the FUV-MAMA/140L flux scale. In all cases the Gemini near-IR spectra over-lapped with the *HST* CCD/750L spectra to allow a relative flux calibration between the two. Here the corrections were $\sim 4-5$ per cent, but larger on the early epochs when the SN flux was brightening rapidly. Information on the final mean spectra can be found in Table 2.

The data were corrected for the recession velocity of M101. For M101 as a whole, this is 241 $\mathrm{km\,s^{-1}}$ (de Vaucouleurs et al. 1991), but the projected radial velocity at the SN site is $\simeq$

[1] IRAF is distributed by the National Optical Astronomy Observatories, which are operated by the Association of Universities for Research in Astronomy, Inc., under cooperative agreement with the National Science Foundation.

Table 1. Log of the *HST* spectroscopic observations of SN 2011fe.

Epoch	MJD observation (days)	Instrument configuration	Total exposure time (s)	Comments
2011-08-28	55801.212	NUV-MAMA/230L	5400	
2011-08-28	55801.100	CCD/430L	1200	CR-SPLIT=3
2011-08-28	55801.117	CCD/750L	1002	CR-SPLIT=3
2011-08-31	55804.304	NUV-MAMA/230L	2200	
2011-08-31	55804.231	CCD/430L	1156	Dither 2x578s w/ CR-SPLIT=2. Saturation.
2011-08-31	55804.244	CCD/750L	410	CR-SPLIT=2. Slight saturation.
2011-09-03	55807.425	CCD/230LB	1320	CR-SPLIT=4.
2011-09-03	55807.438	CCD/430L	195	CR-SPLIT=3. Slight saturation.
2011-09-03	55807.444	CCD/750L	195	CR-SPLIT=3.
2011-09-07	55811.415	CCD/230LB	1060	Dither 2x530s w/ CR-SPLIT=2.
2011-09-07	55811.427	CCD/430L	160	Dither 2x80s w/ CR-SPLIT=2.
2011-09-07	55811.434	CCD/750L	80	CR-SPLIT=2.
2011-09-10	55814.417	CCD/230LB	1060	Dither 2x530s w/ CR-SPLIT=2.
2011-09-10	55814.429	CCD/430L	160	Dither 2x80s w/ CR-SPLIT=2. Slight saturation
2011-09-10	55814.465	CCD/750L	80	CR-SPLIT=2.
2011-09-13	55817.805	FUV-MAMA/140L	8540	
2011-09-13	55817.669	CCD/230LB	830	Dither 2x415s w/ CR-SPLIT=2.
2011-09-13	55817.680	CCD/430L	160	Dither 2x80s w/ CR-SPLIT=2.
2011-09-13	55817.689	CCD/750L	140	Dither 2x70s w/ CR-SPLIT=2.
2011-09-19	55823.661	NUV-MAMA/230L	2720	
2011-09-19	55823.601	CCD/430L	160	Dither 2x80s w/ CR-SPLIT=2.
2011-09-19	55823.608	CCD/750L	70	CR-SPLIT=2
2011-10-01	55835.298	NUV-MAMA/230L	2700	
2011-10-01	55835.231	CCD/430L	1200	Dither 2x600s w/ CR-SPLIT=3. Slight saturation.
2011-10-01	55835.244	CCD/750L	190	CR-SPLIT=2.
2011-10-07	55841.349	NUV-MAMA/230L	3000	Dither 2x1500s
2011-10-07	55841.281	CCD/430L	1320	Dither 2x660s w/ CR-SPIT=3. Slight saturation.
2011-10-07	55841.295	CCD/750L	310	CR-SPLIT=2. Slight saturation.
2011-10-21	55855.210	NUV-MAMA/230L	3000	
2011-10-21	55855.154	CCD/430L	1220	Dither 2x610s w/ CR-SPLIT=2.
2011-10-21	55855.168	CCD/750L	420	CR-SPLIT=2.

Table 2. Details of the mean spectra constructed on each epoch.

Epoch	Ave. MJD observation	Phase (days)[a]	Wavelength coverage
2011-08-28	55801.17	-13.1	1750Å – 2.5μm
2011-08-31	55804.25	-10.1	1750Å – 2.5μm
2011-09-03	55807.38	-6.9	1900Å – 2.5μm
2011-09-07	55811.37	-2.9	1900Å – 2.5μm
2011-09-10	55814.39	+0.1	1900Å – 2.5μm
2011-09-13	55817.67	+3.4	1265Å – 2.5μm
2011-09-19	55823.62	+9.3	1750Å – 1.02μm
2011-10-01	55835.26	+20.9	1750Å – 1.02μm
2011-10-07	55841.31	+27.0	1750Å – 1.02μm
2011-10-21	55855.18	+40.8	1750Å – 1.02μm

[a] The phase is given in days in the SN rest frame relative to maximum light in the rest-frame B-band.

$180\,\mathrm{km\,s^{-1}}$ (Bosma et al. 1981; Patat et al. 2013). We used this latter value in our analysis. We correct for Milky Way (MW) extinction using the maps of Schlegel, Finkbeiner, & Davis (1998) and a Cardelli, Clayton, & Mathis (1989) extinction law. Although it is not clear that these dust maps are reliable near extended objects such as M101, the correction is small (a colour excess $E(B-V)_{\rm mw} = 0.009$ mag) and is consistent with independent evidence from Galactic Na I and Ca II absorption features in high-resolution optical spectra of SN 2011fe (see Patat et al. 2013, who

derive $E(B-V)_{\rm mw} = 0.01$ mag). We discuss extinction caused by dust in the host galaxy in the next section.

Some narrow absorption features, presumably from material in the inter-stellar medium (ISM) along the line of sight to the SN, are present in the UV spectra of SN 2011fe, in particular Mg II at 2796Å and 2803Å, Mg I at 2853Å, Fe II at 2344Å, 2374Å, 2383Å, 2587Å and 2600Å, and various Si II and Al II features in the far-UV. These are at velocities that are consistent with the recession velocity of M101 given the STIS resolution and wavelength calibration accuracy, and are probably associated with the system causing strong Na I absorption at 180 km s^{-1} identified by Patat et al. (2013). We remove the strongest of these lines from the spectra in this paper. The spectra are shown in Fig 1, and are available from the WISeREP archive[2] (Yaron & Gal-Yam 2012).

3 GENERAL PROPERTIES OF SN 2011FE

We now discuss the general optical and UV properties of SN 2011fe. In particular, we assess whether SN 2011fe is broadly representative of other SNe Ia in the UV.

3.1 Photometric properties

M101 was being observed by PTF with a daily cadence around the time of the SN 2011fe discovery. There are non-detection limits of $g > 21.2$ on MJD 55795.2 and $g > 22.2$ on 55796.2, followed by the first detection at $g = 17.3 \pm 0.01$ on MJD 55797.2. The explosion date of SN 2011fe was estimated by N11 by fitting a simple model power-law model to the early-time P48 SN flux, f, as a function of time t, given by $f(t) \propto (t - t_{\rm expl})^n$, where $t_{\rm expl}$ is the explosion time and n is an exponent: $n = 2$ corresponds to a simple 'fireball' model. N11 find $t_{\rm expl} = 55796.687 \pm 0.014$ in MJD (or 2011 August 23.69), with an exponent $n = 2.01 \pm 0.01$.

A significant amount of additional optical photometry of SN 2011fe exists (Richmond & Smith 2012; Vinkó et al. 2012; Munari et al. 2013), and is compared in detail by Pereira et al. (2013). Here, we use the SiFTO light curve fitter (Conley et al. 2008) to fit g photometry from the P48 (as this provides the earliest photometric coverage) and BVR data published by Vinkó et al. (2012). We estimate a time of maximum light in the rest-frame B-band of MJD 55814.30 ± 0.06 (2011 September 10.3), and a peak magnitude in the B-band of 9.93 ± 0.02 mag. The phases of the mean spectra on each epoch can be found in Table 2. SN 2011fe has a SiFTO light curve stretch of 0.98 ± 0.01, and from the SiFTO templates we estimate $\Delta m_{15}(B) = 1.05$ mag – although we caution this number is not a product of SiFTO and is an estimate only. Similar values have been measured by other authors (e.g. Munari et al. 2013). The $B-V$ colour, $\mathcal{C}$, at B-band maximum light is $\mathcal{C} = -0.07 \pm 0.02$. These fit parameters are all fully consistent with independent SALT-II (Guy et al. 2007) fits to SNfactory spectrophotometric data presented by Pereira et al. (2013) and, as discussed by those authors, make SN 2011fe a typical example of a normal SN Ia, and one that would be included in any standard Hubble diagram analysis had it been located in the Hubble flow (see Conley et al. 2011, for a summary of the criteria typically used).

The $B-V$ colour does not provide any evidence for extinction due to the host galaxy; if anything it is slightly blue (cf. figure 1 of Conley et al. 2011). Independent evidence for low extinction comes from Patat et al. (2013), who measure $E(B-V)_{\rm host} = 0.014 \pm 0.002$ mag. We do not correct the data for this small extinction but do account for it in our modelling.

The inferred rise time $t_{\rm r}$ measured from the SN light curve is 17.6 ± 0.1 d, close to the average for normal SNe Ia (Hayden et al. 2010). This is most likely a lower limit to the true $t_{\rm r}$, i.e., the true explosion date is likely earlier than that measured from the light curve: the light-curve based $t_{\rm r}$ measurement does not take into account photon diffusion within the dense ejecta of the young SN. This can lead to a delay between the SN explosion and the emergence of the first optical photons (Piro & Nakar 2013a,b; Hachinger et al. 2013). The rise-time (or explosion date) is a critical input to our modelling as it defines the time from the explosion of the SN to each of our spectra. We assess the consistency of various values of $t_{\rm r}$ with the spectroscopic modelling in Section 5.1.

3.2 UV spectral comparisons

We compare our near-UV spectra of SN 2011fe with the mean near-UV spectrum for low redshift SNe Ia compiled from data in M12 from -1 to +4.5 d. Two of our spectra have phases in this range (Table 2) and we average them together to give a mean phase of +1.8 d. The M12 mean includes SN 2011fe in its construction, so we regenerate the mean without SN 2011fe; the average phase of the mean spectrum is +2.1 d. The comparison is shown in Fig. 2 (left-hand panel). The overall level of agreement is good, although some differences can be seen: for example, the positions/velocities of the near-UV features are systematically redder/slower in SN 2011fe compared to the mean of the M12 sample.

M12 identified a strong trend between the stretch of SNe Ia and the velocities/positions of some near-UV spectral features; higher stretch SNe Ia have bluer features. As SN 2011fe, with $s = 0.98$ (Section 3.1) would fall into the 'low stretch' sample of M12, we also compare to the mean generated from just the low-stretch SNe (Fig. 2, right-hand panel). The agreement between the UV feature positions (particularly the Ca II H&K absorption) is better, and the SN 2011fe spectrum falls within the range of spectra examined in M12.

In summary to this section, we conclude, as have others, that SN 2011fe is photometrically a fairly typical example of a SN Ia, and that this extends to its behaviour in the near-UV. Thus conclusions drawn about this event are likely to be broadly applicable to other SN Ia explosions.

4 MODELLING TECHNIQUES

We now turn to the modelling of the SN 2011fe spectra. We first outline our modelling framework and assumptions, and then present the models of SN 2011fe themselves in Section 5.

4.1 Monte Carlo radiative transfer code

We model the spectra of SN 2011fe using a Monte Carlo code (Abbott & Lucy 1985; Mazzali & Lucy 1993; Lucy 1999; Mazzali 2000; Stehle et al. 2005). The code performs radiative transfer above a sharp lower boundary (or 'photosphere'). To generate a spectrum at any given epoch, the code requires as input the bolometric luminosity $L_{\rm bol}$, the time t since the SN explosion (hence the importance of an accurate knowledge of $t_{\rm r}$), the photospheric

[2] http://www.weizmann.ac.il/astrophysics/wiserep/

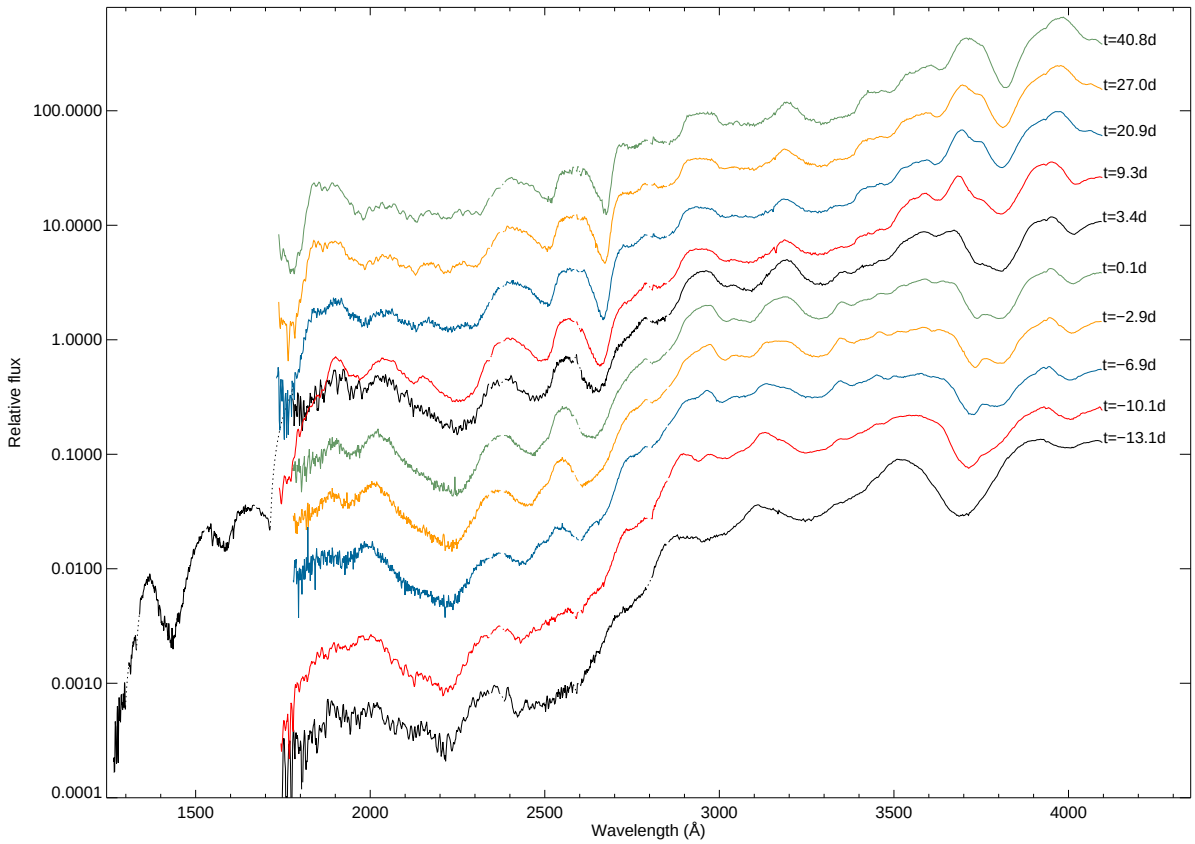

Figure 1. A time-series spectral sequence of the UV portion of the *HST* spectra of SN 2011fe. Spectra have been corrected for Milky Way extinction, corrected to the rest-frame, and had UV ISM absorption lines removed. The phase of each spectrum, marked in days relative to maximum light in the rest-frame B-band, are marked on the right. Each spectrum has been offset arbitrarily for presentation purposes.

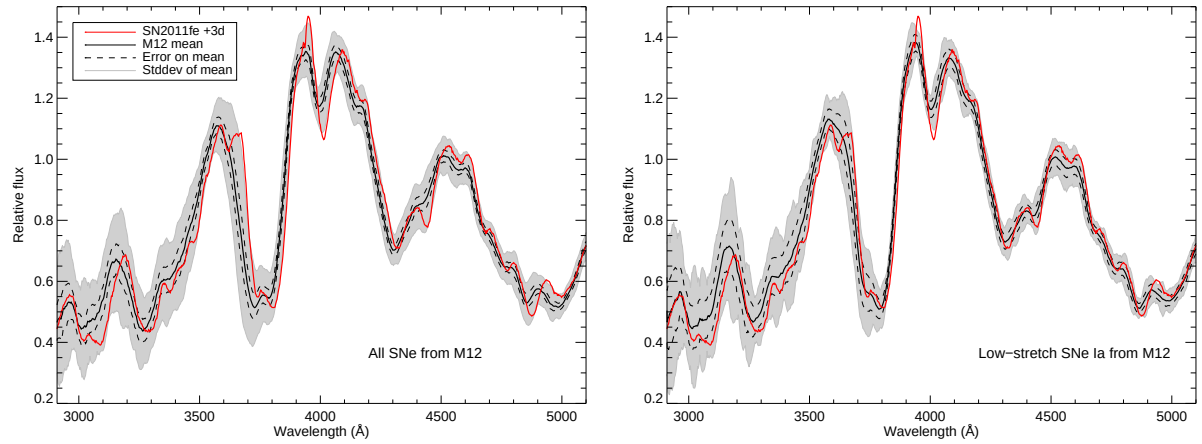

Figure 2. A comparison between the average of the +0.1 d and +3.4 d spectra of SN 2011fe, and the mean near-UV spectrum of M12 constructed from *HST* data taken at phases between -1 and +4.5 d. The dashed line is the error on the M12 mean spectrum, and the shaded grey band shows the standard deviation of the input data. The spectra have been normalised using a box filter between 4000Å and 4500Å. Left: The comparison to the entire M12 sample. Right: The comparison to just the low stretch events ($s < 1.03$).

velocity $v_{\rm ph}$, the density distribution of the SN ejecta in the homologous expansion phase (Section 4.4), and the abundances of the elements in the ejecta.

The code simulates the propagation of photon packets emitted at the photosphere with a black-body spectrum of temperature $T_{\rm ph}$ [$I_\nu^+ = B_\nu(T_{\rm ph})$]. The SN ejecta are assumed to be optically thick below this photosphere. Although this is a relatively rough approximation, and one which at later epochs can cause an excess in the red and IR flux of the models, it makes the code flexible as quantitative abundances can be derived without a knowledge

of the exact distribution of radioactive heating below the photosphere. Since most of the lines important for abundance determination are in the UV/optical, the poor reproduction of the near-IR continuum has only minor consequences on our results. Photon packets undergo Thomson scattering and line absorption. Following absorption, packets are immediately re-emitted in a transition chosen randomly via a branching scheme. Packets that are scattered back into the photosphere are considered to be re-absorbed. Radiative equilibrium is enforced by the 'indivisible-packet' approach (Lucy 1999). The code iterates $T_{\rm ph}$ (and thus the outgoing intensity at the photosphere) so as to match $L_{\rm bol}$ given the actual back-scattering rate.

The excitation/ionisation state of the gas is determined by the radiation field using a modified nebular approximation (Mazzali & Lucy 1993; Mazzali 2000). Starting from an initial guess, the radiation field and the state of the gas are iterated with a series of Monte Carlo experiments until convergence is achieved. The final emergent spectrum is obtained by computing the formal integral, avoiding excessive Poisson noise (Lucy 1999).

4.2 Spectral modelling

In its simplest form, our code uses homogeneous abundances above the photosphere ('one-zone' modelling, e.g. Mazzali et al. 1993). Intermediate-mass elements (IMEs, e.g. Mg, Si, S, Ca) typically influence the strength of spectral features in the optical, whereas Fe-group elements lead to the formation of features in the optical and the UV. Additionally, Fe-group elements are essential for fluorescence and reverse-fluorescence processes, as simulated by the branching scheme (Lucy 1999). These processes can be particularly important for the formation of the UV spectrum (Mazzali 2000).

The spectral line strengths are strongly influenced by ionisation/excitation, which in turn depend on the radiation field. A lower $v_{\rm ph}(= r_{\rm ph}/t)$ leads to a lower $r_{\rm ph}$ and hence a higher temperature with a bluer radiation field at the photosphere, favouring ionisation and the occupation of highly-excited states, with lines forming at lower velocity. A higher $L_{\rm bol}$ has a similar effect on the temperature but not on the line velocities, apart from an indirect effect on ionisation and excitation.

The typical modelling process involves iterating $L_{\rm bol}$ until the flux in the observed spectrum is matched by the model; any IR excess in the model due to the photospheric black-body approximation (Section 4.1) is disregarded. Simultaneously, $v_{\rm ph}$ is iterated to optimise the position of the lines and the overall spectral shape. Abundances are first defined in an approximate way during this process, and may be improved once $L_{\rm bol}$ and $v_{\rm ph}$ are fixed, but since they both depend on the density structure and affect the thermal state of the gas, the two procedures are not physically independent. This also implies that it may be difficult to find a 'perfect' solution. However, the combined fit of line position and strength with the shape of the pseudo-continuum represents a quantitative solution of the physical conditions of the SN atmosphere.

4.3 Abundance tomography

Although one-zone modelling can effectively constrain abundances near the photosphere, it does not follow abundance variations with radius (or velocity). Stehle et al. (2005) introduced the technique of constraining the abundance stratification of the ejecta ('abundance tomography') by using a time series of SN spectra. Defining the abundances as a function of ejecta depth, they used a time series of spectra to 'observe' the different layers.

In the early, photospheric phase (up to a few weeks after maximum light in SNe Ia), the inner ejecta are optically thick. As the ejecta expand, the photosphere recedes inside the ejecta following the decreasing density, as witnessed by the decreasing blueshift of the observed spectral lines (e.g. Benetti et al. 2005). In order to obtain an optimal description of the abundance stratification in the outermost ejecta, two or three independent layers are usually introduced above the photosphere of the first spectrum. The abundances in these layers are defined by fitting the spectrum, with the edges of the layers chosen to improve the fit.

In successive spectra in the time series the photosphere lies at progressively lower velocities. The abundances above the new, lower-lying photosphere (but beneath the previous one) can now be determined. This procedure is repeated with the later spectra until the abundance stratification of the layers accessible with photospheric-epoch spectra is fully described. The process requires iteration: abundances in the outer layers determined from earlier spectra may not be optimal for the later spectra. Thus, the abundances are adapted so as to fit all spectra in the best possible way, re-calculating the entire spectral sequence to obtain a consistent model. The uncertainty in this procedure can be as much as ~ 25 per cent on the abundances, but it is usually smaller (Mazzali et al. 2008).

The inner layers can only be analysed using nebular spectra, which are needed to obtain a complete picture and conclude the abundance tomography procedure (Stehle et al. 2005). The nebular spectra of SN 2011fe will be analysed in a future article.

4.4 Density profiles

One of the most critical ingredients in this process is the assumed density profile of the SN ejecta, which itself is the product of a particular explosion model. For example, a density profile with higher densities in the outer layers of the ejecta can lead to enhanced absorption in the spectral regions sensitive to these layers. The UV is a particularly sensitive region because the large number of overlapping metal lines causes the opacity to be higher than in the optical. Accordingly, we tested various profiles from different explosion models on SN 2011fe. We started with models W7 and WS15DD1 (Nomoto et al. 1984; Iwamoto et al. 1999), as they appear to be the most appropriate for SN 2011fe, which does not show strong absorption at high velocities. These density profiles formally correspond to a single-degenerate explosion scenario; we are not able to test double degenerate scenarios as their density profiles are not available. However, in the outer layers the single and double degenerate profiles are likely to be similar (Pakmor et al. 2012), with the differences revealed only at late times (e.g. Mazzali et al. 2011).

W7 is a parametrised 'fast deflagration' model, with a kinetic energy $E_K = 1.3\ 10^{51}$ erg. Although it may be considered unphysical because of its parametrisations, W7 represents a useful benchmark, and its density distribution has been successfully used to reproduce light curves and spectra of normal SNe Ia (e.g. Stehle et al. 2005; Mazzali et al. 2008). However, delayed-detonation models, where an initial deflagration turns into a supersonic detonation at some point during the explosion (Khokhlov 1991), may be considered more realistic. Although the physics of the transition are still unclear, these models produce explosion energies and abundance stratifications that match SN Ia observations (Mazzali et al. 2007; Tanaka et al. 2011; Röpke et al. 2012). In particular, they pre-expand the white dwarf in the deflagration phase, so that the subsequent detonation produces not only Fe-group elements, but also IMEs, which are ejected at realistic velocities.

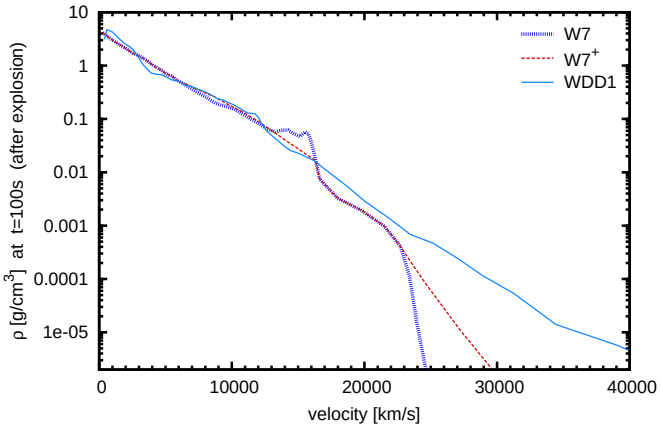

Figure 3. The SN ejecta density profiles of the W7 and WS15DD1 (WDD1) models discussed in Section 4.4 (Iwamoto et al. 1999), and of the W7$^+$ model constructed to optimise the comparison between the synthetic spectra and observed data (Section 5.3).

WS15DD1 (hereafter WDD1) is a low-energy delayed-detonation model (Iwamoto et al. 1999) with $E_K = 1.33\ 10^{51}$ erg and synthesised ^{56}Ni mass $M(^{56}\mathrm{Ni}) = 0.56\,\mathrm{M}_\odot$, which is a good match to values derived from the bolometric light-curve of SN 2011fe (Pereira et al. 2013).

Our models are most sensitive to the density profile outside the core (i.e. the outer $\Delta M \sim 0.5\,\mathrm{M}_\odot$), and thus for our modelling the important difference between W7 and WDD1 is the amount of material at high velocity (see Fig. 3). This is larger in WDD1, reflecting the passage of the detonation shock. Based on the effect density profiles have on the UV, we also construct a third, 'intermediate' density profile which yields better fits to the spectra than either W7 or WDD1. We call this model 'W7$^+$' (Section 5.3), and also show it in Fig. 3.

5 SPECTRAL MODELLING OF SN 2011FE

Our goal is to model the spectral data for SN 2011fe using the framework outlined in Section 4. Our base models assume a metallicity of 0.5 $Z_\odot$, motivated by the metallicity of M101 at the position of SN 2011fe (Stoll et al. 2011). We explore this assumption in Section 6.1.

The first step is to determine the rise time (t_r) from the models independently from the t_r measured from the photometry (Section 3.1). This requires very early spectral data, where the leverage on the explosion epoch is largest and the statistical uncertainty consequently smallest (Mazzali 2000) – a small absolute change in t_r is large in relative terms. We make use of an early low-resolution spectrum taken with the Telescopio Nazionale Galileo (TNG) on 2011 August 25 (MJD 55798.8) and previously presented in N11 and analysed in Parrent et al. (2012). The value of t_r that provides the best fit is then used to model the spectra at later epochs.

We have opted not to use two earlier spectra of SN 2011fe that are also available (see Parrent et al. 2012). The LT and Lick spectra of 2011 August 24 are affected by high velocity features (HVFs). These are weak compared to other SNe Ia (Mazzali et al. 2005, e.g.) and are not detached from the photospheric component, but do cause a significant blueshift of the observed features (Parrent et al. 2012). This makes it difficult to locate precisely the position of the photosphere, and hence to produce accurate models, without a detailed knowledge of the ejecta properties that lead to the generation of these HVFs. We defer this more complex analysis to a later paper.

5.1 Testing the rise time

Early-time spectra of SNe can be used to estimate the time of the explosion (Mazzali & Schmidt 2005). The combination of L_bol, temperature (which depends on L_bol and radius r), and velocity of the absorption lines (which depends on r and t) can give powerful constraints on t_r. For both the W7 and WDD1 profiles, we computed spectral models on epochs ranging from 2.3 to 5.3 d, corresponding to rise times from 17.6 d (N11), which we regard as a lower limit, to 20.6 d, in steps of 0.5 d. A selection of these different t_r models is shown in Fig. 4. The different assumed epochs require different values of v_ph. The line velocities reflect the time evolution of the density profile, and thus in particular the assumed t_r (Hachinger et al. 2012). For a larger t_r, the spectra will be at older epochs in the SN evolution, and thus the ejecta density in the model will be lower; v_ph is therefore lower and the lines less blueshifted. Note that v_ph is not exactly inversely proportional to t, as would be predicted by a simple Stefan-Boltzmann law. In models with higher t or lower v_ph (i.e. a photosphere deeper in the density profile, which rises steeply inwards) the back-scattering rate of photons would be strongly increased if one assumed $v_\mathrm{ph} \sim t^{-1}$. Therefore, a realistic photosphere for such a model, avoiding an excessive temperature increase at the photosphere (via strong back-warming to maintain the outwards photon flux), must lie at a higher velocity.

For the August 25 spectrum, v_ph lies between ∼11000 and 18000 km s^{-1}, depending on density profile and t_r. We chose values that yield the same radiation temperature at the photosphere (T_ph) in all models with the same density profile: ∼10800 K for models based on W7 and ∼10300 K for models based on WDD1. This ensures that the ionisation/excitation state is similar in all models. Two abundance zones were used above v_ph, with the boundaries between these zones at 19400 km s^{-1} for W7 and at 18100 km s^{-1} for WDD1. Abundances were optimised for the models with t_r=19 d and not further modified; this has only a minor influence on the results.

The optimum t_r is taken as the one where the line positions in the model spectra best match the line positions in the observations. This is only possible if the lines measured do not exhibit strong HVFs (Mazzali et al. 2005). In the TNG spectrum the HVFs are present only in the Ca lines, and we exclude these from our t_r determination.

We measured the positions[3] of several features that are well reproduced in the model spectra (marked in Fig. 4) in addition to Si II λ6355 and O I λ7773 (cf. Hachinger et al. 2009, 2012). Table 3 gives the wavelength offset $\Delta\lambda = \lambda_\mathrm{model} - \lambda_\mathrm{obs}$ for the two different models and the spectral features. Fitting a regression line to the $\overline{\Delta\lambda}$–t_r relation (where $\overline{\Delta\lambda}$ is the mean offset of the features at fixed t_r), we determine the value of t_r for which $\overline{\Delta\lambda} = 0$. We obtain an optimum t_r of 19.0 d for W7 and 19.6 d for WDD1, with

[3] Line-positions are measured as a line centroid wavelength, calculated as $\lambda_c = \frac{\int_{\Delta\lambda} FD^3(\lambda)\lambda \mathrm{d}\lambda}{\int_{\Delta\lambda} FD^3(\lambda)\mathrm{d}\lambda}$, where $FD^3(\lambda)$ is the third power of the fractional depth at λ (cf. Hachinger et al. 2008), and the integrals run over the range $\Delta\lambda$ in which the line absorbs. We use the centroid instead of the deepest point (as was done, for example, in Hachinger et al. 2008) as the centroid can be more reliably determined when feature shapes are irregular and show considerable fluctuations among the model series, as is the case for our very early-epoch models here.

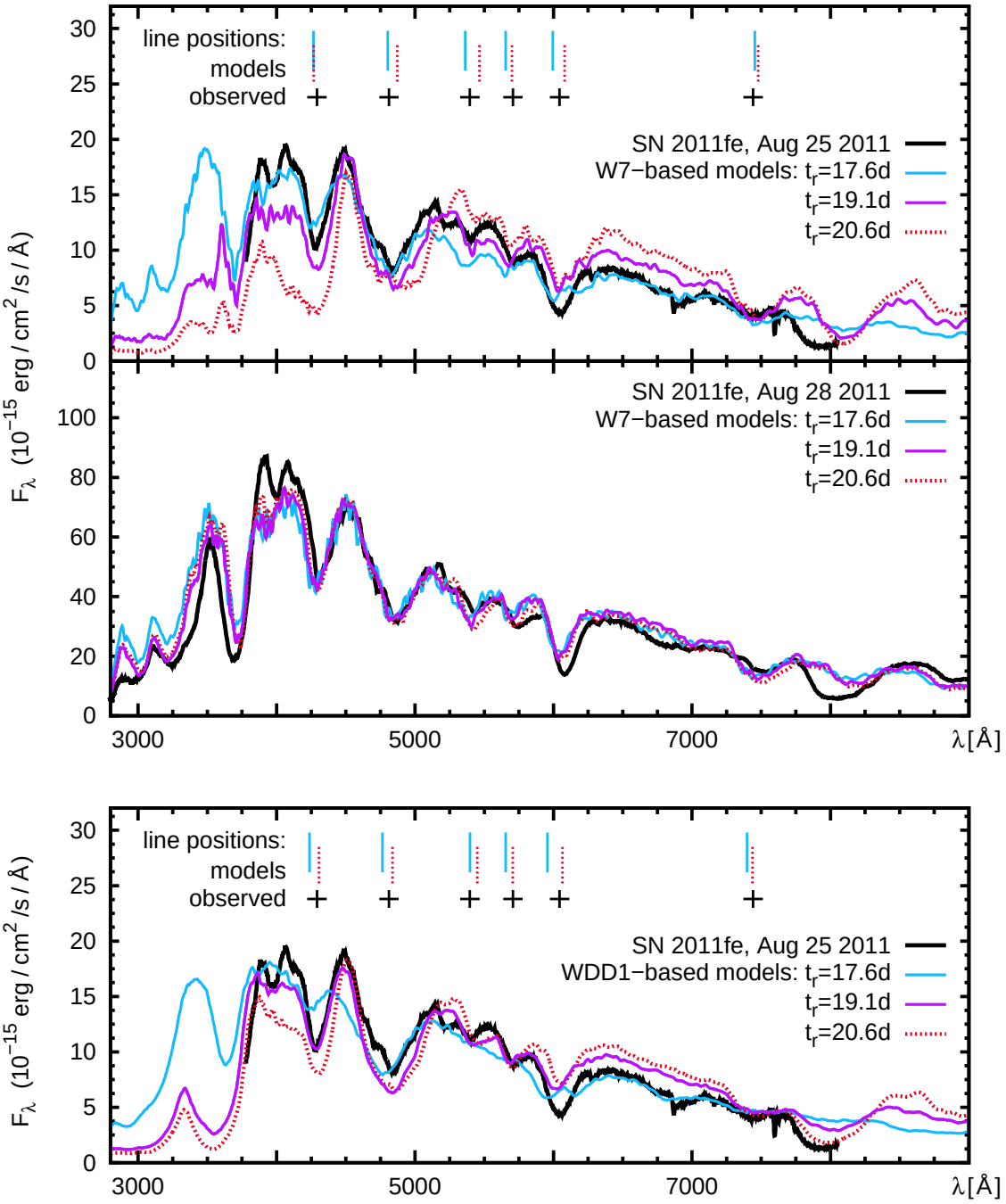

Figure 4. Early-time models for SN 2011fe computed for rise times t_r ranging from 17.6 to 20.6 d. Models in the *upper panel* were computed with the W7 density profile, models in the *lower panel* are based on WDD1. The best-fitting t_r is determined from the 2011 August 25 spectrum, where t_r has the largest effect: the middle panel shows the W7 models for the 2011 August 28 spectrum, which are less sensitive to t_r. The positions of prominent features in the spectra are marked as black crosses, and the corresponding model features also marked. For t_r=17.6 d, the model spectral features are on average too blue; this is no longer the case when a longer t_r is used.

a statistical error of $\simeq 0.5$ d in both cases. The relation $\overline{\Delta\lambda}$–t_r in Table 3 is non-monotonic on a scale $\Delta t_r \lesssim 0.5$ d, but on larger time scales it is well-behaved.

The quality of the spectral models depends on the entire feature shape, and not just on the match in the measured wavelength. Models computed for a short (17.6 d) and a long (20.6 d) t_r clearly do not match the data. Those with a long t_r are too red, reflecting the fact that the photospheric radius is comparatively large when maintaining a reasonable back-scattering rate. Those with a short t_r tend to have high v_{ph} and consequently show features that are too blueshifted and weak, as the mass above the photosphere is too small.

Although the optimum t_r does depend on the density profile used, it is always larger than 17.6 d by $\gtrsim$1 d. This suggests that SN 2011fe exploded earlier than inferred by fitting a power-law model to the early light curve. This delay is a simple effect of pho-

Table 3. Rise time (t_r) determination from fits to the 2011 August 25 SN 2011fe spectrum, with the offset between synthetic and observed spectral features, $\Delta\lambda = \lambda_{\rm model} - \lambda_{\rm obs}$ and the average offset, $\overline{\Delta\lambda}$. The fact that features do not always follow the overall trend of being less blueshifted for larger t_r reflects the uncertainties in determining model line velocities.

t_r	$\Delta\lambda$(Fe / Mg $\sim$4300 Å) (Å)	$\Delta\lambda$(Fe / etc. $\sim$4800 Å) (Å)	$\Delta\lambda$(S II λ5640) (Å)	$\Delta\lambda$(S II λ5972) (Å)	$\Delta\lambda$(Si II λ6355) (Å)	$\Delta\lambda$(O I λ7773) (Å)	$\overline{\Delta\lambda}$ (Å)
W7-based models							
17.6	−25.5	−8.3	−32.9	−53.1	−49.4	11.7	−26.3
18.1	−16.1	−1.3	−20.8	−41.1	−28.0	7.1	−16.7
18.6	−4.1	9.1	4.8	−34.2	−18.5	8.6	−5.7
19.1	8.3	18.3	9.6	−30.5	4.6	9.4	3.3
19.6	−3.8	34.0	13.6	−18.9	4.6	15.7	7.5
20.1	−3.7	60.6	39.2	−17.3	24.6	30.6	22.3
20.6	−23.3	59.4	69.6	−7.0	36.4	36.3	28.6
regression line fit to $\overline{\Delta\lambda}$–t_r relation $\Rightarrow$ $\overline{\Delta\lambda} \simeq 0$ for $t_{r,W7} \simeq$19.0 d							
WDD1-based models							
17.6	−53.9	−46.8	0.5	−52.4	−87.1	−43.6	−47.2
18.1	−33.2	−27.2	−16.0	−48.4	−68.1	−21.4	−35.7
18.6	−17.9	−18.0	−7.3	−37.1	−44.6	−14.2	−23.2
19.1	−2.8	−4.4	24.3	−26.8	−17.8	0.8	−4.5
19.6	8.5	8.7	45.0	−21.2	−4.6	2.0	6.4
20.1	8.8	15.0	42.5	−11.2	13.3	−15.1	8.9
20.6	14.4	25.9	53.5	−1.6	20.3	−4.8	18.0
regression line fit to $\overline{\Delta\lambda}$–t_r relation $\Rightarrow$ $\overline{\Delta\lambda} \simeq 0$ for $t_{r,WDD1} \simeq$19.6 d							

ton diffusion: visible light is produced by the thermalisation of the γ-rays and the deposition of the energy of the positrons emitted in the decay of ^{56}Ni. At early phases, when the density is high, these processes take place essentially locally in the region where ^{56}Ni dominates, typically in the deeper layers of the ejecta. Optical photons must then diffuse out of the ejecta before they can be observed. This requires time, given the high density and consequently high opacity in the inner ejecta.

We conclude that while a fit to early light curve data can only set a lower limit on t_r, with spectral modelling it is possible to improve this estimate. The accuracy of the result depends on the availability of early spectral data. However, in the presence of any HVFs that affect the spectra, standard explosion models that are unable to reproduce these HVFs make it difficult (if not impossible) to determine t_r without a detailed modelling of the outermost layers of the SN ejecta (Tanaka et al. 2008).

5.2 W7- and WDD1-based spectral models

Having used an early spectrum to determine t_r, we now analyse the *HST* time series using the W7 and WDD1 densities (Figs. 5 and 6, respectively). The model parameters are compiled in Table 4. Note that we do not use the last three *HST* spectra (Table 2), as our code is optimised for the early photospheric phase, around and prior to maximum light, and these spectra have epochs larger than 20 days after peak.

For the spectrum of 2011 August 25 we used $v_{\rm ph}$ as used in the models for the t_r determination. For W7 we used an epoch $t = 3.7$ d and $v_{\rm ph} = 14350\,{\rm km\,s^{-1}}$, and for WDD1 $t = 4.3$ d and $v_{\rm ph} = 12450\,{\rm km\,s^{-1}}$. Despite the very early epoch and the high $v_{\rm ph}$, strong Si II lines are visible, indicating the presence of burned material in the outer layers. In order to reproduce these lines, our models require > 30 per cent by mass of the ejecta above $v_{\rm ph}$ to be material heavier than oxygen in the W7-based model. This is only $\sim$13 per cent in the WDD1-based model. Most of the burned material consists of IMEs ($9 \leqslant Z \leqslant 20$), but traces of Fe-group elements are also present. Line blanketing in the UV, which is mostly due to overlapping lines of Fe-group elements, is much stronger in the WDD1-based model than in the W7-based one, as the delayed-detonation places more material at high velocity. The delayed-detonation model yields a better reproduction of the peak around 4000 Å, although neither matches the feature well. This may be a consequence of our assumption of black-body emission at the photosphere. However, more sophisticated models that do not make that assumption also have difficulties reproducing this high peak, which is seen in several SNe Ia. Overall, both models reproduce the observed features reasonably well except for Si II λ6355, which is too weak in both models. However, increasing the Si abundance above the photosphere to correct this then results in too much high-velocity Si absorption in the later epoch models. In the Ca II IR triplet hints of a HVF are visible, confirmed in later epochs. As discussed above, we do not try to match these HVFs, although they may be the reason for the strength of the Si II line in this spectrum.

Note that $v_{\rm ph}$ is larger in the W7 model than in the WDD1 one. This may seem counter-intuitive, as W7 has less mass at high velocity. The reason for selecting a higher $v_{\rm ph}$ for W7 is that because of the smaller mass at high velocity, the UV opacity is smaller and hence the UV flux higher than in WDD1 if similar $v_{\rm ph}$ are used. By selecting a higher $v_{\rm ph}$ the temperature is reduced and the UV flux decreases. This is obviously not an ideal solution, since the line velocities are then too high, but it shows that W7 does not have the correct density distribution at high velocities.

On 2011 August 28 the first UV spectrum was observed by *HST*. Having the UV available constrains our models significantly. While both density profiles provide a good fit in the optical, the

Table 4. Luminosities, photospheric velocities and temperatures of the photospheric black-body in the W7 and WDD1 models.

Date (UTC)	Phase (days)	t (days)	$L_{\rm bol}$ ($10^9 L_\odot$)	$v_{\rm ph}$ (km s^{-1})	$T_{\rm ph}$ (K)
		W7			
Aug. 25	−15.5	3.7	0.08	14350	10800
Aug. 28	−13.1	5.7	0.32	13250	12450
Aug. 31	−10.1	9.0	1.1	11300	14650
Sept. 3	−6.9	12.1	2.3	10400	15100
Sept. 7	−2.9	16.1	3.2	8600	15100
Sept. 10	+0.1	19.1	3.5	7600	14600
Sept. 13	+3.4	22.4	3.2	6500	14050
Sept. 19	+9.3	28.3	2.3	4600	13600
		WDD1			
Aug. 25	−15.5	4.3	0.08	12450	10300
Aug. 28	−13.1	6.3	0.32	11750	12250
Aug. 31	−10.1	9.6	1.1	10650	14300
Sept. 3	−6.9	12.7	2.3	10100	14600
Sept. 7	−2.9	16.7	3.2	8600	14900
Sept. 10	+0.1	19.7	3.5	7550	14700
Sept. 13	+3.4	23.0	3.2	6200	14450
Sept. 19	+9.3	28.9	2.3	4500	13450

synthetic spectra show large differences in the UV. In particular, the low flux level at $\lesssim$2500 Å can only be reproduced if there is sufficient material above the photosphere to absorb photons, which is a feature of delayed-detonation models. Features in the UV are dominated by singly-ionised Fe-group elements and Mg (Fig. 5). Ni, Fe, Ti / V / Cr[4] and Mg influence different parts of the spectrum, so that their abundances can be determined independently. These different UV features are discussed in more detail in Section 5.3.

The next two spectra were obtained on 2011 August 31 and 2011 September 3 ($\sim$ 9–13 d after explosion) when the SN was significantly more luminous. Between 2700 and 3500 Å, absorption by doubly-ionised Fe-group species now appears. The photosphere is now in the incompletely burned region (10100-11300 km s^{-1}), where the two models differ less in density. At both epochs, the synthetic spectra match the observed ones reasonably well. Most differences are in the UV. The positions of the UV features of the W7 model agree with the observed ones, but the overall flux is generally too high, implying too little absorbing material, as discussed above. The WDD1-based model reproduces the overall flux, but the Fe-group lines are too blueshifted because of the increased high-velocity absorption introduced by even a weak delayed-detonation model. In both models, the regions just above the photosphere contains a mass fraction of up to 6 per cent of Fe (this is so high that it is likely to be Fe synthesised in the explosion), while the mass fraction of ^{56}Ni, including the decay products ^{56}Co and ^{56}Fe (which is however negligible at this early phase), is between 11 and 30 per cent. The dominant constituents in this region are, however, IMEs. The carbon abundance at these velocities has dropped to zero. A weak C II line may still be present at ~ 6580Å in the observations: this can be reproduced by the carbon in the outer layers.

By maximum light (the 2011 September 7 and 2011 September 10 spectra; Fig. 6), the photosphere has receded about half way inside the ejecta ($v_{\rm ph} \sim 7550 - 8600$ km s^{-1}). The value of $L_{\rm bol}$ at maximum is in good agreement with that derived by Pereira et al. (2013). In these layers ^{56}Ni dominates, and little incompletely burned or unburned material remains. In the UV, where the fit is very good, Co lines play a larger role as ^{56}Ni decays. The slight mismatch between models and observations in the red and IR, where the models show a small flux excess, is likely a consequence of the black-body approximation at the photosphere (Section 4.1).

At post-maximum epochs, (2011 September 13 and 19, $\sim$23 and 29 d after explosion, respectively, Fig. 6), the largest differences between the W7 and WDD1 models are again in the UV. The W7-based model now gives a somewhat better match. In the near-UV, the absorptions of the WDD1-based model are too blue and the UV flux too low, again indicating too much opacity at high velocities. The WDD1-based model is in better agreement with the data in the far-UV ($\lambda < 2000$ Å) in the 2011 September 13 spectrum, the only epoch for which far-UV data are available. However, it may be affected by too much back-warming, again a consequence of the large mass at high velocities: this can be seen in the excessive Si III 5740 Å absorption.

The September 19 spectrum can be modelled using a photospheric velocity of 4600 km s^{-1} for W7 or 4500 km s^{-1} for WDD1. The material at this depth is very rich in ^{56}Ni, and a more reliable analysis of these zones should be made using nebular spectra.

5.3 The hybrid 'W7$^+$' model

Having assessed the spectral fits resulting from the W7 and WDD1 density profiles, we now construct a third density model (W7$^+$) with the aim of yielding improved model fits to the data. Specifically, we attach a high-velocity tail to the W7 model, but with lower densities and a steeper decline in the density profile at high velocities when compared to WDD1. The physical motivation is to avoid the excessively high velocities of the UV features in the WDD1 models, while increasing the opacity at high velocities with respect to W7 and thus yielding a better match to the UV flux level.

We implement the high-velocity tail as a smooth power-law extension to W7, with

$$\rho(r) = \rho_0 \times (\frac{r}{r_0})^{-20}$$

above $r_0 = 23000$ km s^{-1} $\times$ t, with $\rho_0 = 3.2 \times 10^{-4}$ g cm^{-3} (at a reference time of 100 s after explosion). In addition, between 10000 and 16000 km s^{-1} we smoothed the density profile to mimic explosion models where a detonation wave runs through these layers (Fig. 3). This smoothing has no major effects on the spectra. W7$^+$ has a $E_K = 1.18 \times 10^{51}$ erg, where the bulk of the ejecta at $v < 16000$ km s^{-1}carries less energy than the corresponding zone in W7 (1.03 vs. 1.15×10^{51} erg). The high-velocity tail of W7$^+$ has little mass and only carries a relatively small amount of energy. In essence, W7$^+$ can be compared to a very weak delayed detonation.

As a first check of W7$^+$, we performed the same rise-time test as for W7 and WDD1 (Section 5.1), setting $T_{\rm ph} = 10450$ K. Synthetic spectra for the different rise times are shown in Fig. 7 and the line offsets are given in Table 5. We infer an optimum rise time of $t_{\rm r} = 19.0 \pm 0.5$ d, similar to the values obtained for W7 and WDD1, and subsequently model the spectral time series using this value.

The synthetic spectra for the model series are shown in Figs. 8

[4] The lines of Ti, V, and Cr are too heavily blended for us to be able to distinguish the influence of each element. Therefore we determined a combined abundance, with a mix similar to the results of nucleosynthesis models (Iwamoto et al. 1999).

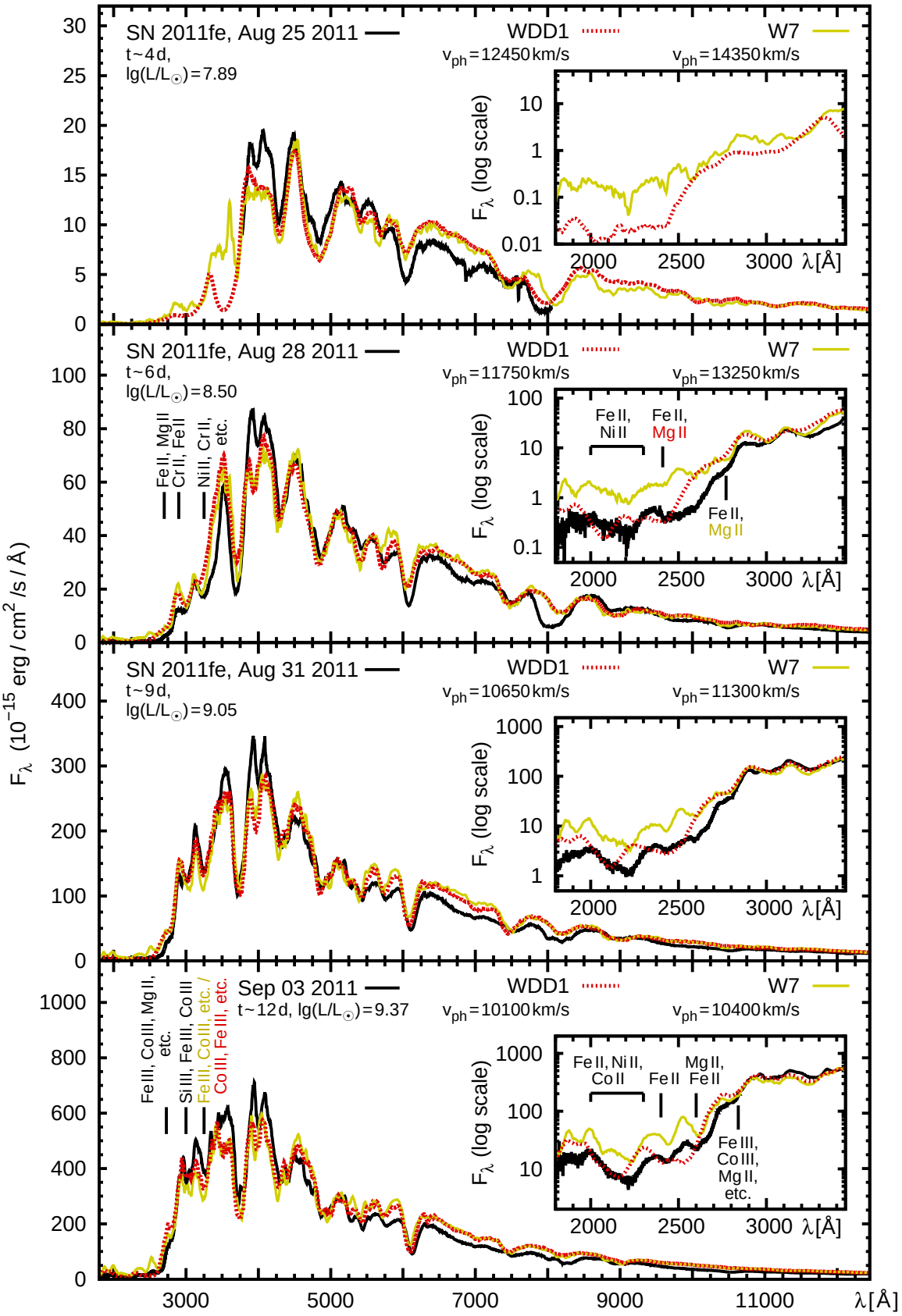

Figure 5. Spectra of SN 2011fe (black lines) compared to models based on the W7 and WDD1 density profiles (yellow / light grey, solid lines; red / grey, dotted lines, respectively). Insets show the UV in more detail (with logarithmic flux axis). The models have been reddened by $E(B-V)_{\rm host} = 0.014$ mag. The ions responsible for the most prominent UV features in our model are marked, in order of importance.

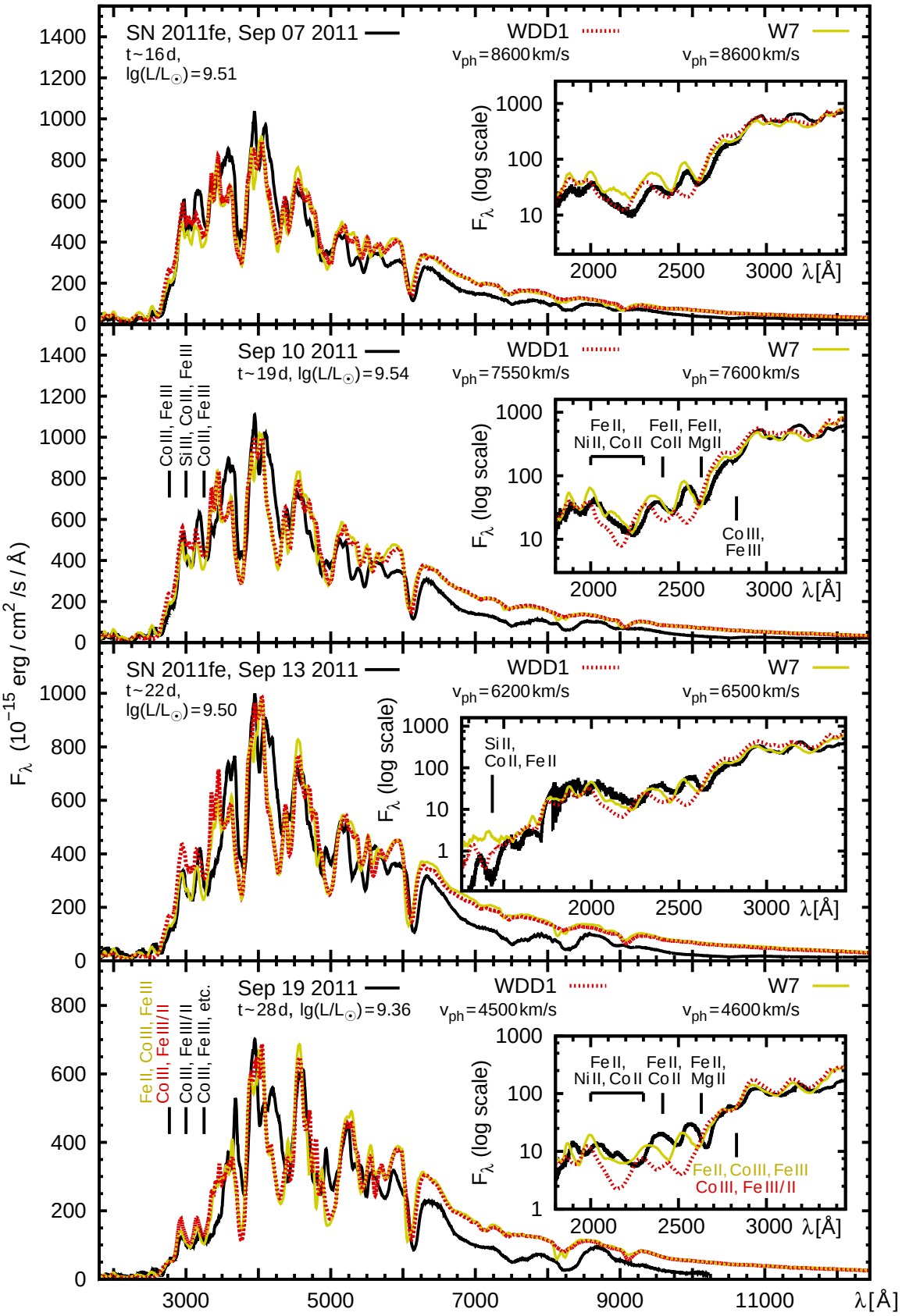

Figure 6. The W7 and WDD1 model sequences, continued.

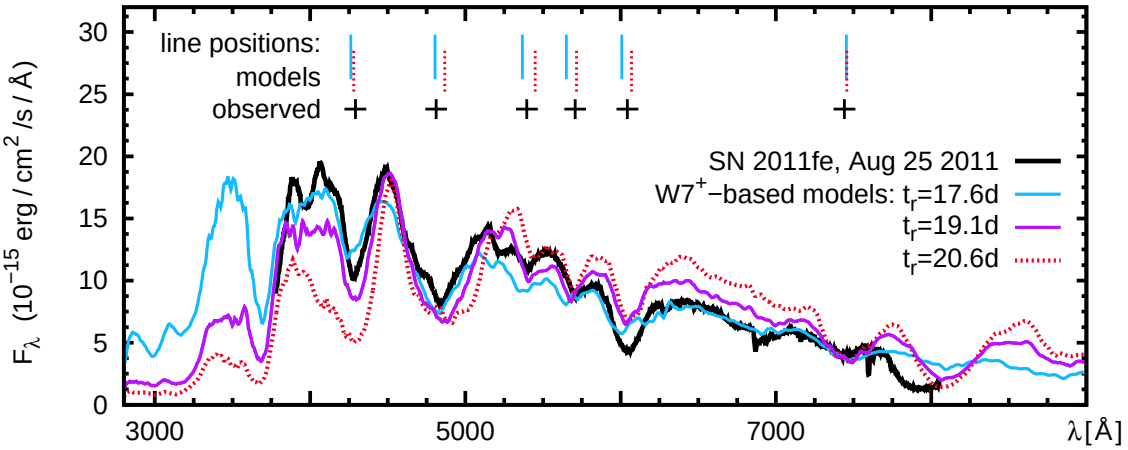

Figure 7. Early-time models for SN 2011fe based on the W7$^+$ density profile, assuming different rise times t_r between 17.6 d and 20.6 d. The optimum rise time is determined comparing the positions of prominent features in the optical between observed spectrum (black crosses) and models (purple/grey, solid lines for 17.6 d; red/dark grey, dotted lines for 20.6 d) – analogous to Fig. 4.

Table 5. As Table 3, but for the W7$^+$ model.

t_r	$\Delta\lambda$(Fe / Mg $\sim$4300 Å) (Å)	$\Delta\lambda$(Fe / etc. $\sim$4800 Å) (Å)	$\Delta\lambda$(S II λ5640) (Å)	$\Delta\lambda$(S II λ5972) (Å)	$\Delta\lambda$(Si II λ6355) (Å)	$\Delta\lambda$(O I λ7773) (Å)	$\overline{\Delta\lambda}$ (Å)
W7$^+$-based models							
17.6	−29.3	−7.4	−28.4	−57.2	−36.5	11.9	−24.5
18.1	−17.3	5.6	−16.6	−43.4	−30.6	8.8	−15.6
18.6	−5.0	6.6	−2.5	−35.5	−14.0	7.0	−7.2
19.1	4.4	17.0	14.8	−24.6	−0.7	18.9	5.0
19.6	9.3	26.3	35.6	−12.5	5.7	18.2	13.8
20.1	6.2	31.3	55.6	−8.0	16.3	20.9	20.4
20.6	−11.0	55.1	53.2	9.0	26.1	15.3	24.6
regression line fit to $\overline{\Delta\lambda}$–t_r relation $\Rightarrow$ $\overline{\Delta\lambda} \simeq 0$ for $t_{r,\mathrm{W7}^+} \simeq 19.0$ d							

and 9, with the model parameters and physical properties listed in Table 6). As expected, the W7$^+$ model spectra are intermediate between the W7 and WDD1 spectra. The largest differences are in the UV, although several features in the optical are also improved.

At the earliest epochs (2011 August 25 and 2011 August 31), W7$^+$ shows stronger UV absorption than W7, although the continuum level still lies above the data, while the shapes of the UV spectral features are better reproduced than in WDD1. In general, W7$^+$, with its moderate high-velocity ejecta tail, reproduces the position of the prominent features in the UV (Figs. 8 and 9). In particular, the position of the Ni/Co/Fe-dominated trough near 2000–2300 Å is better reproduced at all pre-maximum epochs. However, at all pre-maximum epochs the flux level in the UV is too high and the absorption features are somewhat too narrow. The implication is that the real density will deviate from the power-law shape of W7$^+$ at high velocities (i.e. more mass may be required, although less than in WDD1). We defer an accurate study of this issue, including the modelling of HVFs, to later work.

Given a density profile that yields improved fits to the shape of the UV (and optical) spectral features, in principle we can now diagnose abundances more precisely. The Ni/Co/Fe blend near 2000–2300 Å is a diagnostic for radioactive material from the ^{56}Ni $\rightarrow$ ^{56}Co $\rightarrow$ ^{56}Fe decay chain, and its shape shows some sensitivity to ^{56}Ni even in the outer ejecta. Fe directly synthesised in the explosion can be constrained from Fe-dominated features such as the near-UV blend near 3300 Å and from the optical Fe features. Thus, as discussed in the following sections, the UV spectra allow us to constrain the Fe and ^{56}Ni abundances (cf. Hachinger et al. 2013) not only in the outermost layers but also in the inner, intermediate layers.

Table 6. Luminosities, photospheric velocities and temperatures of the photospheric black-body in the W7$^+$ model (analogous to Table 4).

Date (UTC)	Phase (days)	t (days)	L_{bol} ($10^9 L_\odot$)	v_{ph} (km s^{-1})	T_{ph} (K)
W7$^+$					
Aug. 25	−15.5	3.7	0.08	13850	10450
Aug. 28	−13.1	5.7	0.32	12750	12250
Aug. 31	−10.1	9.0	1.1	11250	14400
Sept. 3	−6.9	12.1	2.3	10450	14850
Sept. 7	−2.9	16.1	3.2	9000	14750
Sept. 10	+0.1	19.1	3.5	7700	14750
Sept. 13	+3.4	22.4	3.2	6200	14700
Sept. 19	+9.3	28.3	2.3	4550	13750

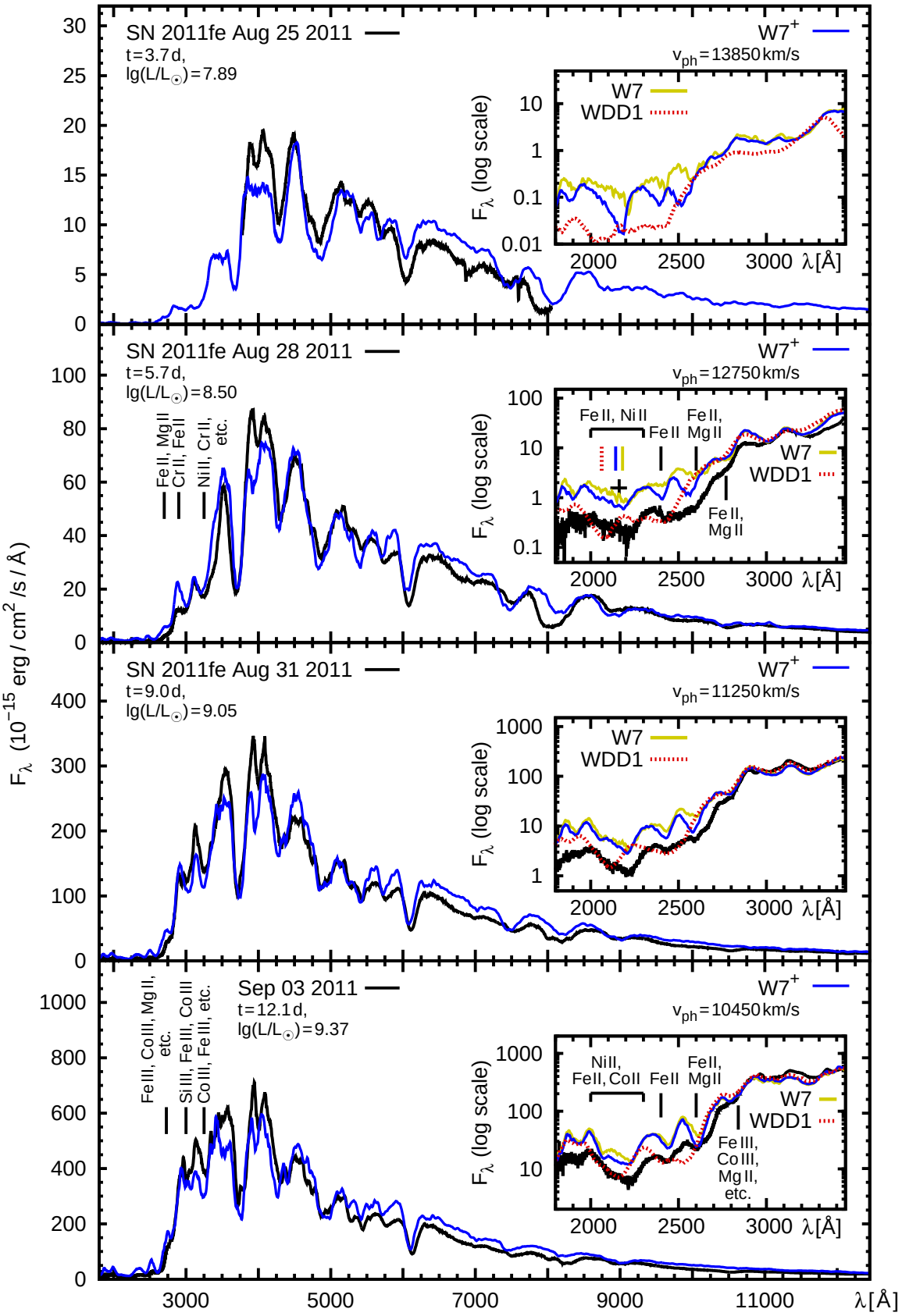

Figure 8. Spectra of SN 2011fe (black lines) compared to models based on the W7^{+} density profile (blue, solid lines). The insets also show the W7-based models (yellow, solid lines) and the WDD1-based models (red, dotted lines) for comparison. The inset for Aug 28 demonstrates that W7^{+} reproduces the observed position of UV features (as does W7 in general), while WDD1 does not: the centroid wavelength of the observed feature around 2000–2300 Å is marked with with a cross, while lines mark the position in the different models.

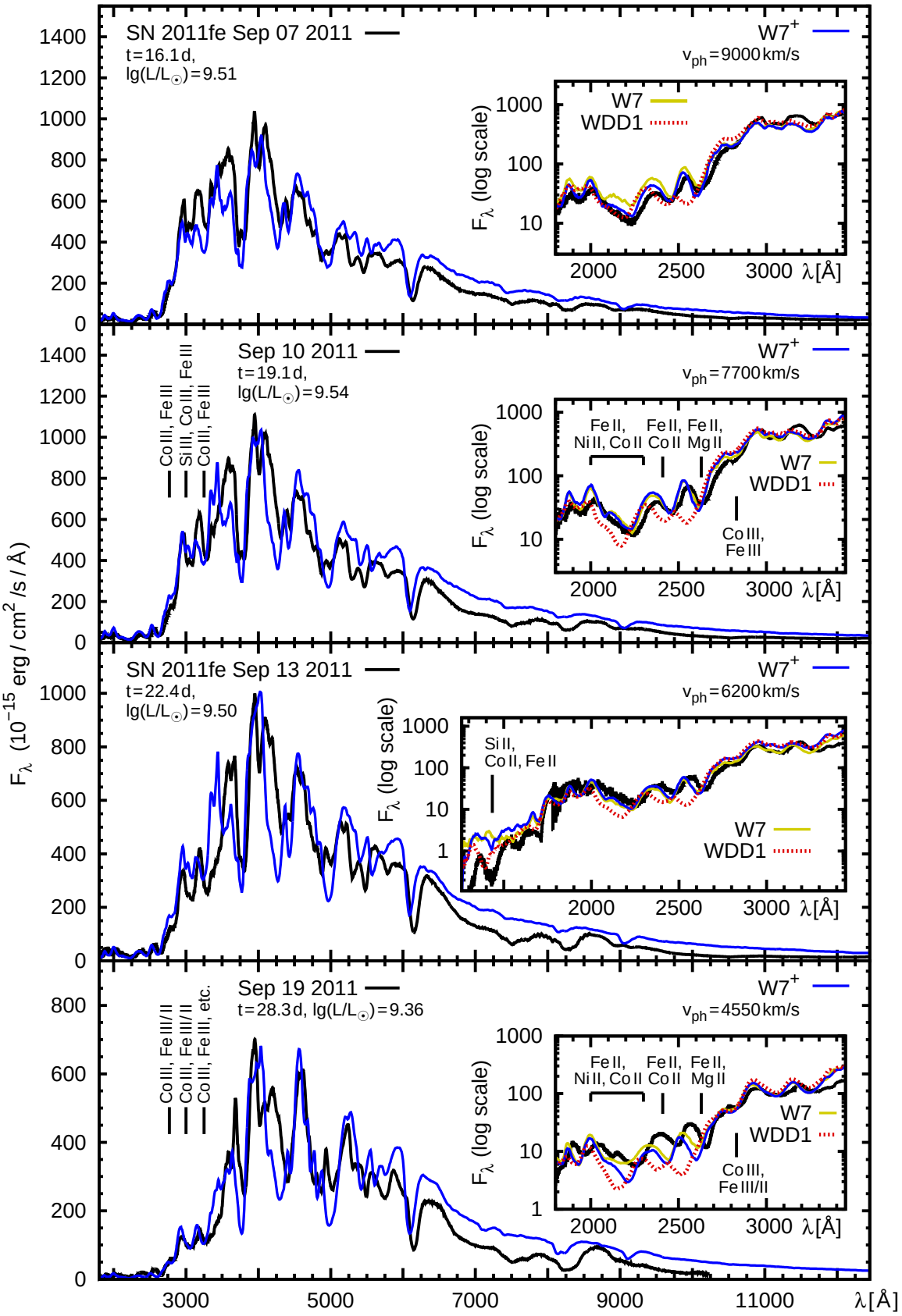

Figure 9. The W7^{+} model sequence, continued.

5.4 Abundances

The abundance stratification we infer for SN 2011fe using the W7$^+$ profile is shown in Fig. 10. It has similarities to the results of the W7 nucleosynthesis calculations (Iwamoto et al. 1999; Fig. 10), but there are significant differences in the degree of mixing, in particular at intermediate velocities.

A thin outer layer above $\sim$19400 km s^{-1} introduced as an extra abundance zone above the August 25 photosphere, containing $\sim$0.01 M$_\odot$, is composed almost exclusively of carbon (98 per cent by mass). A higher oxygen abundance in these layers would lead to spurious absorption in the blue wing of the O I λ7773 feature, as discussed in Section 6.3. We tested the sensitivity of the models to the Fe abundance in the outermost layers, and found that a sub-solar abundance gives the best results (see Sect. 6.1). This is consistent with the metallicity of M101 (Stoll et al. 2011).

The layer immediately below ($16000 < v \leqslant 19400$ km s^{-1}) contains predominantly oxygen (87 per cent by mass). Some IMEs (e.g. Si, 6 per cent) and the first traces of ^{56}Ni (0.1 per cent including decay products ^{56}Co and ^{56}Fe) are also present, as is directly-synthesised Fe (0.1 per cent) and other Fe-group elements, but the carbon abundance is low. These heavier elements are required in order to reproduce the observed lines in the August 25 spectrum.

The layer at $13850 < v \leqslant 16000$ km s^{-1} contains a higher fraction of burning products, including Si (20 per cent by mass), directly-synthesised Fe (0.2 per cent), and ^{56}Ni (0.2 per cent).

In the zones between 10450 and 13850 km s^{-1}, IMEs dominate the composition. Among these, Si is the most abundant, as expected. Below 10450 km s^{-1}, IMEs start to decrease, and ^{56}Ni becomes the dominant species. Its abundance reaches $\sim$ 30 per cent at that velocity and it increases at lower velocities. The abundance of stable Fe near 10000 km s^{-1} appears to be somewhat smaller than in W7, but this is compensated by the higher abundance of ^{56}Ni. This may be regarded as an indication of a sub-solar metallicity of the progenitor.

The photosphere of the last spectrum analysed here is at 4550 km s^{-1}. Below this velocity a core of $\sim$ 0.3 M$_\odot$ should exist, which can analysed by modelling the nebular spectra (e.g. Stehle et al. 2005). Above this velocity we find 0.5 M$_\odot$ of ^{56}Ni in a total mass of $\sim$ 1.1 M$_\odot$. As we cannot establish the exact composition of the core or its mass based on the analysis of the photospheric-phase spectra only (see for example Mazzali et al. 2011; Mazzali & Hachinger 2012), we can only state that our model may contain 0.5–0.8M$_\odot$ of ^{56}Ni. This is in good agreement with the W7 and WDD1 models, and with the ^{56}Ni mass estimate from the bolometric luminosity of SN 2011fe (0.53 ± 0.11 M$_\odot$; Pereira et al. 2013).

6 DISCUSSION

6.1 Fe-group abundances and progenitor metallicity

The distribution of Fe-group elements in SNe Ia largely determines their light curves and greatly affects their spectra. It is therefore a key element when comparing theoretical models to observations (e.g. Mazzali 2000; Mazzali et al. 2001, 2007; Röpke et al. 2007; Pfannes et al. 2010). Different SN Ia explosion models (deflagrations, delayed detonations, double-degenerate mergers) with different progenitor metallicities will differ in their average ^{56}Ni and stable Fe-group yield and/or in the distribution of these elements. Observations of SNe Ia with good temporal and spectral coverage make it possible to diagnose this Fe-group content with high precision (e.g. Stehle et al. 2005; Stritzinger et al. 2006; Tanaka et al. 2011; Hachinger et al. 2013).

Earlier studies suggested that the UV may be the spectral region from which the stratification of ^{56}Ni and other Fe-group elements in the outer layers of the SN can be determined in most detail (e.g. Lentz et al. 2000; Walker et al. 2012; Hachinger et al. 2013). Very early light-curve data may also help in this respect (Piro & Nakar 2013b). Foley & Kirshner (2013) derived a sub-solar abundance for the progenitor of SN 2011fe by evaluating models of Lentz et al. (2000) and employing a semi-empirical argument based on the metallicity dependence of the amount of ^{56}Ni versus stable Fe-group elements produced in the explosion. However, this method neither fully accounts for the different ^{56}Ni production in SNe Ia with different luminosities at fixed progenitor metallicity, nor for the actual Fe-group opacities in SN 2011fe, which can differ from the opacities used in the standard models of Lentz et al. (2000). Here, with our detailed models for SN 2011fe, we can directly investigate the metal content of the outer-lying ejecta regions, where nucleosynthesis is expected to play a minor role and the progenitor metallicity is still reflected in the Fe-group content.

We tested the Fe-group content in the outermost layers by recomputing the W7$^+$-based spectral models, and modifying the Fe-group abundances in these layers ($v > 19400$ km s^{-1}). We find (Fig. 11) that the effect of changing the metallicity is stronger in the UV but more linear in the optical, probably because the latter is less saturated.

The Fe-dominated absorption at $\sim$4800Å in the August 25 spectrum is too strong in the model with solar metallicity (Fig. 11, top panel, inset). This absorption is still present if $Z = 0$, and thus is mostly due to Fe located near the photosphere at 13900 km s^{-1}; Si and Mg also contribute. All models show too much flux at $\lambda \lesssim 3000$ Å. We believe this reflects remaining shortcomings of W7$^+$, as discussed below. Models with outer layer Fe-group abundances corresponding to the M101 metallicity, $Z \simeq 0.5 Z_\odot$, and with $0.25 Z_\odot$, give reasonable matches. They show less absorption in the optical Fe feature (which makes them preferable over the $Z_\odot$ model), while the flux level at UV wavelengths does not increase significantly. Models with a $0.1 Z_\odot$ Fe-group abundance, or with progenitor metallicity of zero, have a higher UV flux on August 28 at $\lambda \lesssim 3000$ Å, and in addition do not match the shape of the optical Fe feature on August 25. We therefore consider them less optimal.

The excess flux in the far-UV at $\lambda \lesssim 3000$ Å, present in all our models, probably cannot be avoided with the explosion models we have used, even if a super-solar metallicity in the outermost layers is assumed. This high flux is presumably the result of reverse-fluorescence photons emitted in outer layers (cf. Sauer et al. 2008a), such that the emerging flux cannot be effectively absorbed. Only WDD1 models do not suffer from this, because they have more mass at high velocity to absorb the flux. It is then likely that a density bump at the highest velocities, or at least a region with a significantly higher density, but with a different distribution in velocity than WDD1, may simultaneously reproduce the HVFs, the UV continuum and the shapes of the UV features. Studying this is outside the scope of the present paper, but clearly remains an interesting focus for future work.

As a general remark, the sensitivity of the UV spectra on the (virtually) unburned outer layer will crucially depend on that layer's extent. This is evident when comparing the present work with our earlier study of maximum-light spectra (Walker et al. 2012), where a larger fraction of the ejecta was considered un-

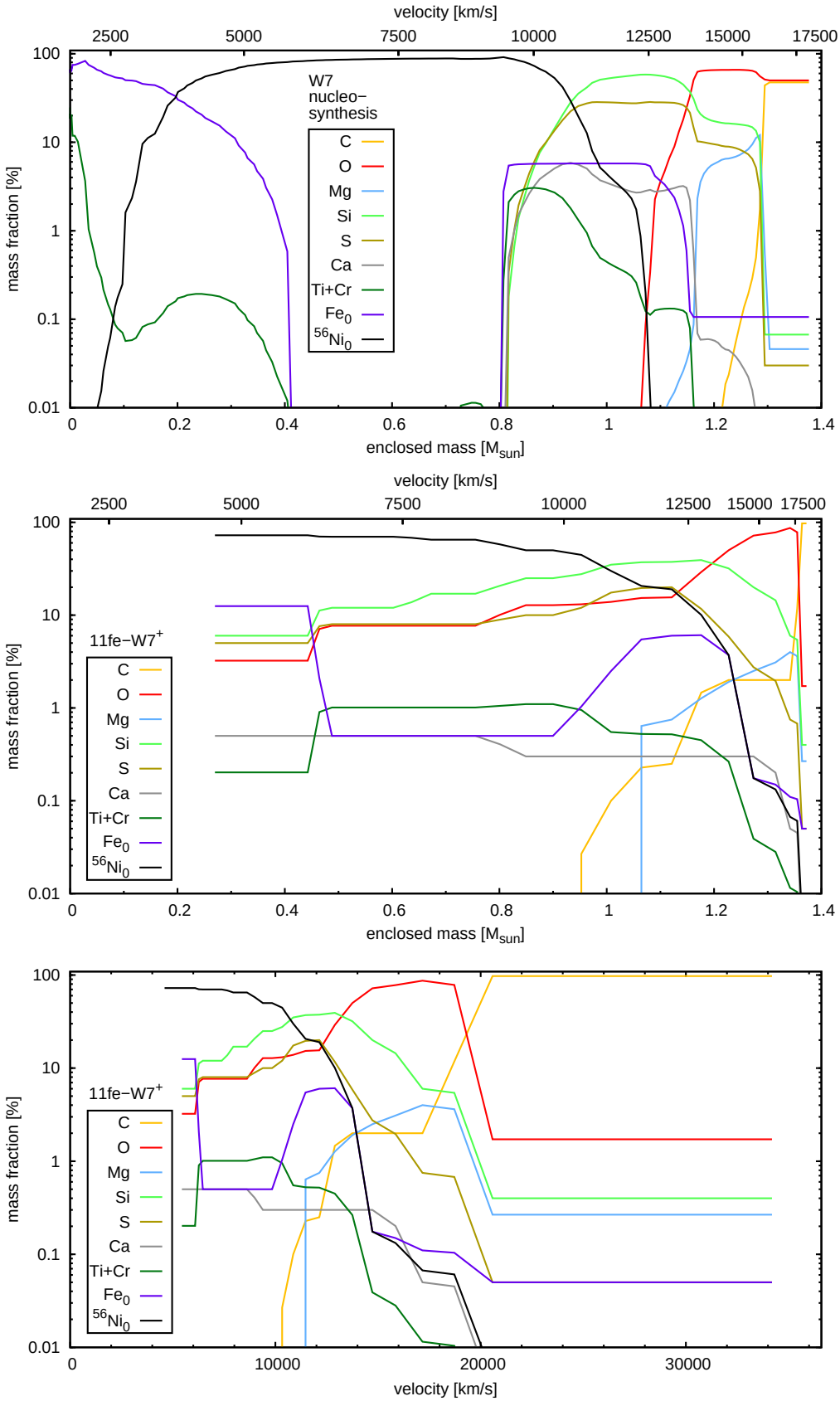

Figure 10. Abundances of W7 nucleosynthesis calculations (Iwamoto et al. 1999, *top panel*, plotted in mass space), compared to our tomography based on W7^{+} (the *middle panel* shows mass space, the *lower panel* is in velocity space). The Ni/Co/Fe abundances are given in terms of the mass fractions of ^{56}Ni and stable Fe at $t = 0$ [$X(^{56}\mathrm{Ni}_0)$, $X(\mathrm{Fe}_0)$]; stable Ni and Co are present only in traces (few per cent or less by mass) in our model.

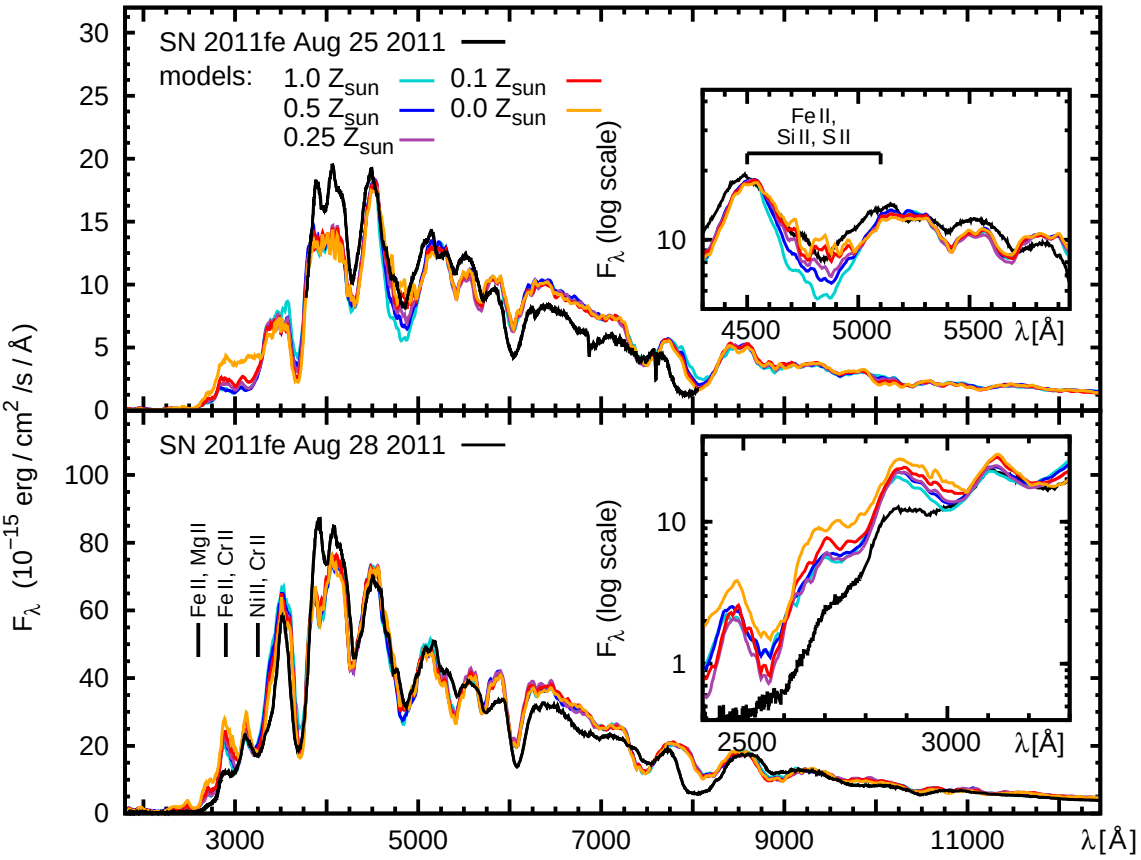

Figure 11. Effect of Fe-group abundances in the outermost layers: earliest spectra of the W7$^+$ model sequence, and synthetic spectra computed for different Fe-group abundances in the outermost layers ($v > 19400\,\mathrm{km\,s^{-1}}$). The insets show the UV in more detail for Aug 28 and the Fe-dominated blend around 4800 Å for Aug 25.

burned and thus more closely tracked the progenitor metallicity, with a stronger spectral dependence on the abundance modification. On the other hand, the UV spectra can be used to diagnose the Fe-group composition in the incompletely-burned layers ($10000 - 12000\,\mathrm{km\,s^{-1}}$), where we find ^{56}Ni and directly-synthesised Fe in almost equal parts (Section 5.4). The composition in these layers appears to lie between the solar-metallicity model W7 (where only Fe is produced in partially-burned layers because of excess neutrons in ^{22}Ne) and the zero metallicity explosion model 'W70' (Iwamoto et al. 1999). This indirectly suggests a moderately sub-solar metallicity of the progenitor of SN 2011fe.

6.2 Estimate of rise-time and constraints on the progenitor system

Spectral modelling can be used to estimate the epoch of early spectra through the combined fitting of temperature and line velocity. Our results indicate that the rise-time is larger than estimated by simple analytical fits to the light curve, regardless of the model used. This confirms that radiation transport delays the rise of the curve. Such a delay was already derived for SN 2010jn (1.0 d; Hachinger et al. 2013). This was a bright SN Ia, so ^{56}Ni should be found closer to the surface than in SN 2011fe, which was a more rapid decliner. The diffusion time of the first photons should therefore be smaller, and the delay smaller. The slightly larger delay in SN 2011fe (1.4 d) is consistent with a smaller ^{56}Ni mass, and with ^{56}Ni being located deeper in the ejecta.

The assumed rise time t_r has implications for the constraints on the progenitor radius determined from the earliest light-curve points. N11 used their earliest light-curve point (MJD 55797.2) and the earlier non-detections (Section 3.1), together with the analytical early-emission models of Rabinak et al. (2012) and Kasen (2010), to constrain the progenitor radius to $R_\mathrm{prog} \lesssim 0.1\,\mathrm{R}_\odot$. Bloom et al. (2012, hereafter B12) refined this limit, taking into account a later non-detection ($g > 19.0$ at MJD 55796.9) from PIRATE on the Open University's 0.4 m telescope in Mallorca. B12 derived $R_\mathrm{prog} \lesssim 0.02\,\mathrm{R}_\odot$.

In our W7$^+$ model, the optimum-fit explosion time is 1.4 d earlier than the date inferred by N11 giving an explosion epoch of MJD 55795.3. This is consistent with the non-detection on MJD 55795.2, and is then 0.9 d before the next non-detection on 55796.2 giving time for any shock-heated cooling to have faded (Piro & Nakar 2013b). Following the analysis of B12 and using the equations of Rabinak & Waxman (2011), we derive $R_\mathrm{prog} \lesssim 0.02\,\mathrm{R}_\odot$, a very similar constraint to B12. That is, a non-detection of $g > 19.0$ at 4 h after explosion formally gives similar constraints as a non-detection of $g > 22.2$ at 21 h after explosion.

However, as discussed by Rabinak, Livne, & Waxman (2012) and B12, the expressions used for the early SN luminosity from Rabinak & Waxman (2011) assume that the post-shock pressure is dominated by radiation. When the shock diffusion front reaches shells dominated by plasma pressure, a sharp drop in the luminosity is expected. The timing of this drop is proportional to the progenitor star radius (Rabinak et al. 2012), and so this effectively places a

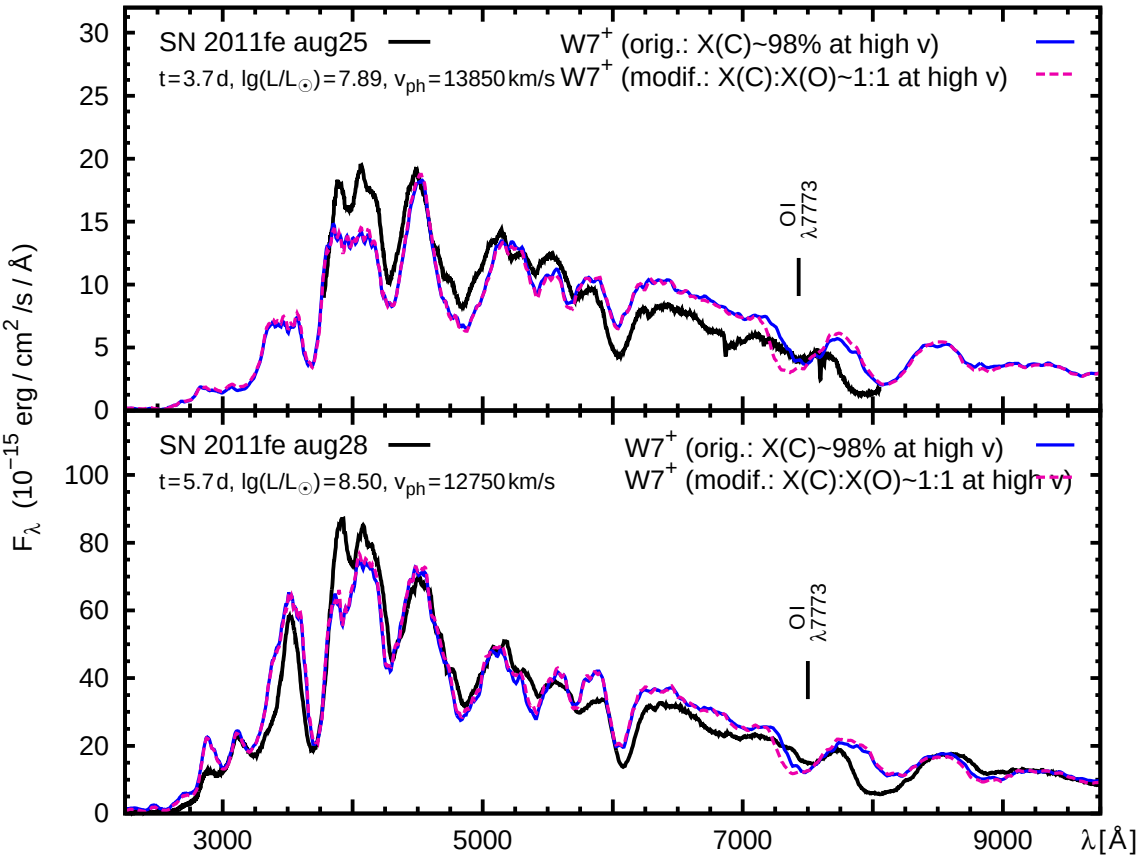

Figure 12. Effect of oxygen in the outermost layers of the model: the earliest two spectra of the SN 2011fe (black) compared to W7^{+} models. The model where the outer layer is almost exclusively composed of carbon ($\sim$ 98 per cent by mass, blue / grey, solid lines) fits the observed O I λ7774 line. A modified model with equal C and O abundances at $v > 19400$ km s^{-1} (red / grey, dotted lines) has too much high-velocity absorption in the O I λ line.

lower limit on the progenitor radius constraint (B12). At 4 h after explosion this limit is $< 0.02\,R_{\odot}$ (B12), but by 21 h after explosion this rises to $\sim 0.06\,R_{\odot}$ – we cannot probe below this limit. Thus, with our new explosion date determination, the resulting limits on the progenitor size are broadly similar to those presented by N11, and a factor of a few larger than B12.

6.3 Carbon layer

Our models require a carbon-dominated outermost layer, at $v > 19400$ km s^{-1} (Fig. 10). The presence of this layer is supported by the influence carbon has on the spectra: the carbon feature near 6600 Å disappears quickly, which requires carbon to be located at a high velocity. The presence of some heavier elements, consistent with the metal content of the progenitor, is also necessary. On the other hand, oxygen has a negative effect on the spectra: if half of the carbon is replaced by oxygen at these high velocities, the O I 7774 Å line is too strong and blue (Fig. 12).

This outermost layer should most directly reflect the properties of the accreting material. There may be two scenarios in which an outer carbon-rich layer can develop. The first is via accretion of hydrogen (in a single degenerate system). This hydrogen can convert into carbon, but the time-scale for subsequent conversion into oxygen may be too short. A second scenario is via accretion of helium, with the helium then burning to carbon – but this is more unlikely as helium tends to burn explosively. Thus we qualitatively favour the hydrogen-accretion scenario. Directly detecting this hydrogen, which should be located at high velocities, would be the key to confirming this, but hydrogen lines may require non-thermal excitation (Hachinger et al. 2012), which is not very strong in the first few days after explosion when the optical depth to the γ-rays produced by ^{56}Ni decay deep in the SN is still very large (Mazzali & Lucy 1998) and small amounts of hydrogen may go undetected. On the other hand, some indirect evidence for the presence of a small amount of hydrogen comes from the presence of HVFs (Altavilla et al. 2007). HVFs are weak in SN 2011fe, but not absent (see also Parrent et al. 2012). In a future publication we will study in more detail the possible upper limits to the hydrogen mass.

7 SUMMARY AND CONCLUSIONS

We have analysed a series of photospheric-epoch UV and optical spectra of the nearby, moderately luminous SN Ia SN 2011fe. The spectra can be reproduced using a 'modified W7' model ('W7^{+}'), which has a higher density in the outer layers than the standard W7 model. Our models suggest that the explosion may have been a weak delayed detonation explosion of a white dwarf accreting hydrogen from a non-degenerate companion. The abundance stratification we infer agrees with ^{56}Ni mass estimates of $\sim 0.5 M_{\odot}$ in the literature.

The focus of this study was to infer the abundance distribution in SN 2011fe. Some ^{56}Ni is present at relatively high velocities. This seems to be a common property of SNe Ia (Mazzali et al.

2008). Stable iron and other iron-group elements in the outermost layers, where burning is weak or absent, should be good tracers of the properties of the progenitor white dwarf. The Fe-group content in these layers determined by our models is consistent with a sub-solar metallicity in the progenitor. The relative iron-group abundances inferred in the incompletely-burned zones, where iron and ^{56}Ni are present in roughly equal amounts, also seems to indicate a sub-solar metallicity (cf. Iwamoto et al. 1999).

In a recent study, Piro & Nakar (2013b) investigated the implications of different ^{56}Ni abundance distributions on the early light curve. In qualitative agreement with their study, we find that the ^{56}Ni distribution in SN 2011fe has a high-velocity tail, but abundances are very small in the outermost $0.1\mathrm{M}_{\odot}$ of the ejecta. This implies that the SN had a 'dark time' between explosion and emission of the first optical light (cf. Piro & Nakar 2013b). Our spectral analysis is sensitive to this dark time via the time-dependent density distribution. We find that a dark time of ~ 1.4 d is required – a somewhat longer value than the ~ 0.5 d found by Piro & Nakar (2013b) in their light-curve analysis. As outlined by Piro & Nakar (2013b), this dark period has implications on the upper limits on the radii of the progenitor ($R_{\rm prog}$) determined from the early light-curve (Nugent et al. 2011; Bloom et al. 2012): we find $R_{\rm prog} \lesssim 0.06\,\mathrm{R}_{\odot}$.

UV spectra are an important tool to determine progenitor metallicities and understanding spectral and light-curve properties of different SNe Ia: depending on the exact ^{56}Ni distribution and on the presence of other iron-group elements, the opacity of objects with the same luminosity can vary (Timmes et al. 2003; Mazzali & Podsiadlowski 2006). This may, for example, explain why SNe with similar luminosity show different evolution of their line velocities (Höflich et al. 2010). It will be important to obtain UV spectral series for other SNe Ia in the future.

This work was made possible by the availability of a high-quality time series of UV-optical spectra. We have inferred explosion properties, including abundances, and crafted a density model that improves the spectra fits, in particular in the UV. This model still has shortcomings, and it is by no means the ultimate solution. However, it demonstrates what can be learned using spectral modelling as a method to investigate all properties of the explosion, not just composition. It would be interesting to determine whether a model similar to ours can be obtained from first principles. Cross-fertilisation between observations, modelling and first-principles calculations of stellar evolution and explosion is the only way to make real progress in our physical understanding of SNe Ia.

ACKNOWLEDGEMENTS

This work is based on observations made with the NASA / ESA Hubble Space Telescope, obtained at the Space Telescope Science Institute, which is operated by the Association of Universities for Research in Astronomy, Inc., under NASA contract NAS 5-26555. These observations are associated with program #12298. Based on observations made with the Italian Telescopio Nazionale Galileo (TNG) operated on the island of La Palma by the Fundación Galileo Galilei of the INAF (Istituto Nazionale di Astrofisica) at the Spanish Observatorio del Roque de los Muchachos of the Instituto de Astrofisica de Canarias. We would like to thank the TNG staff for their support. PAM and SH acknowledge support from the Italian Space Agency under programme ASI-INAF I/009/10/0. MS acknowledges support from the Royal Society. Research by AG is supported by grants from the BSF, the EU via an FP7/ERC grant, the ARCHES prize and the Kimmel Award for Innovative Investigation. Collaborative work between AG and PAM is supported by the Minerva foundation. We have made use of the NASA/IPAC Extragalactic Database (NED, http://nedwww.ipac.caltech.edu, operated by the Jet Propulsion Laboratory, California Institute of Technology, under contract with the National Aeronautics and Space Administration).

REFERENCES

Abbott D. C., Lucy L. B., 1985, ApJ, 288, 679
Altavilla G., et al., 2007, A&A, 475, 585
Astier P., 2012, Rep. Prog. Phys., 75, 116901
Balland C., et al., 2009, A&A, 507, 85
Benetti S., et al., 2005, ApJ, 623, 1011
Bloom J. S., et al., 2012, ApJ, 744, L17
Bosma A., Goss W. M., Allen R. J., 1981, A&A, 93, 106
Branch D., Venkatakrishna K. L., 1986, ApJ, 306, L21
Bufano F., et al., 2009, ApJ, 700, 1456
Cappellaro E., Turatto M., Fernley J., 1995, ESA SCIENTIFIC PUBLICATION ESA-SP 1189, 1189
Cardelli J. A., Clayton G. C., Mathis J. S., 1989, ApJ, 345, 245
Conley A. et al., 2011, ApJS, 192, 1
Conley A., et al., 2008, ApJ, 681, 482
de Vaucouleurs G., de Vaucouleurs A., Corwin, Jr. H. G., Buta R. J., Paturel G., Fouqué P., 1991, Third Reference Catalogue of Bright Galaxies. Volume III: Data for galaxies between 12^h and 24^h. Spinger, New York, (USA)
Ellis R. S., et al., 2008, ApJ, 674, 51
Foley R. J. et al., 2008a, ApJ, 684, 68
Foley R. J., Filippenko A. V., Jha S. W., 2008b, ApJ, 686, 117
Foley R. J., Kirshner R. P., 2013, ApJ, submitted (arXiv:1302.4479)
Foley R. J., et al., 2012a, AJ, 143, 113
Foley R. J., et al., 2012b, ApJ, 753, L5
Foley R. J., et al., 2012c, ApJ, 744, 38
Guy J. et al., 2007, A&A, 466, 11
Hachinger S., Mazzali P. A., Tanaka M., Hillebrandt W., Benetti S., 2008, MNRAS, 389, 1087
Hachinger S., Mazzali P. A., Taubenberger S., Fink M., Pakmor R., Hillebrandt W., Seitenzahl I. R., 2012, MNRAS, 427, 2057
Hachinger S., Mazzali P. A., Taubenberger S., Pakmor R., Hillebrandt W., 2009, MNRAS, 399, 1238
Hachinger S., et al., 2013, MNRAS, 429, 2228
Hayden B. T., et al., 2010, ApJ, 712, 350
Hoeflich P., Wheeler J. C., Thielemann F. K., 1998, ApJ, 495, 617
Höflich P. et al., 2010, ApJ, 710, 444
Howell D. A., 2011, Nature Communications, 2
Hsiao E. Y. et al., 2013, ApJ, 766, 72
Iwamoto K., Brachwitz F., Nomoto K., Kishimoto N., Umeda H., Hix W. R., Thielemann F., 1999, ApJS, 125, 439
Jeffery D. J., Leibundgut B., Kirshner R. P., Benetti S., Branch D., Sonneborn G., 1992, ApJ, 397, 304
Kasen D., 2010, ApJ, 708, 1025
Kessler R., et al., 2009, ApJS, 185, 32
Khokhlov A. M., 1991, A&A, 245, 114
Kirshner R. P. et al., 1993, ApJ, 415, 589
Law N. M., et al., 2009, PASP, 121, 1395
Leibundgut B., Kirshner R. P., Filippenko A. V., Shields J. C., Foltz C. B., Phillips M. M., Sonneborn G., 1991, ApJ, 371, L23
Lentz E. J., Baron E., Branch D., Hauschildt P. H., Nugent P. E., 2000, ApJ, 530, 966

Lucy L. B., 1999, A&A, 345, 211
Maguire K. et al., 2012, MNRAS, 426, 2359
Mazzali P. A., 2000, A&A, 363, 705
Mazzali P. A., Hachinger S., 2012, MNRAS, 424, 2926
Mazzali P. A., Lucy L. B., 1993, A&A, 279, 447
Mazzali P. A., Lucy L. B., 1998, MNRAS, 295, 428
Mazzali P. A., Lucy L. B., Danziger I. J., Gouiffes C., Cappellaro E., Turatto M., 1993, A&A, 269, 423
Mazzali P. A., Maurer I., Stritzinger M., Taubenberger S., Benetti S., Hachinger S., 2011, MNRAS, 416, 881
Mazzali P. A., Nomoto K., Cappellaro E., Nakamura T., Umeda H., Iwamoto K., 2001, ApJ, 547, 988
Mazzali P. A., Podsiadlowski P., 2006, MNRAS, 369, L19
Mazzali P. A., Röpke F. K., Benetti S., Hillebrandt W., 2007, Sci, 315, 825
Mazzali P. A., Sauer D. N., Pastorello A., Benetti S., Hillebrandt W., 2008, MNRAS, 386, 1897
Mazzali P. A., Schmidt B. P., 2005, in IAU Symposium, Vol. 201, New Cosmological Data and the Values of the Fundamental Parameters, Lasenby A. N., Wilkinson A., eds., p. 241
Mazzali P. A., et al., 2005, ApJ, 623, L37
Munari U., Henden A., Belligoli R., Castellani F., Cherini G., Righetti G. L., Vagnozzi A., 2013, New Astronomy, 20, 30
Nomoto K., Thielemann F., Yokoi K., 1984, ApJ, 286, 644
Nugent P. E. et al., 2011, Nature, 480, 344
Pakmor R., Kromer M., Taubenberger S., Sim S. A., Roepke F. K., Hillebrandt W., 2012, ApJ, accepted (ArXiv:1201.5123)
Parrent J. T., et al., 2012, ApJ, 752, L26
Patat F., et al., 2013, A&A, 549, A62
Pereira R., et al., 2013, ArXiv e-prints
Perlmutter S., et al., 1999, ApJ, 517, 565
Pfannes J. M. M., Niemeyer J. C., Schmidt W., Klingenberg C., 2010, A&A, 509, A74
Piro A. L., Nakar E., 2013a, ApJ, submitted (arXiv:1210.3032)
Piro A. L., Nakar E., 2013b, ApJ, submitted (arXiv:1211.6438)
Rabinak I., Livne E., Waxman E., 2012, ApJ, 757, 35
Rabinak I., Waxman E., 2011, ApJ, 728, 63
Rau A., et al., 2009, PASP, 121, 1334
Richmond M. W., Smith H. A., 2012, Journal of the American Association of Variable Star Observers (JAAVSO), 40, 872
Riess A. G., et al., 1998, AJ, 116, 1009
Riess A. G., et al., 2007, ApJ, 659, 98
Röpke F. K., Hillebrandt W., Schmidt W., Niemeyer J. C., Blinnikov S. I., Mazzali P. A., 2007, ApJ, 668, 1132
Röpke F. K. et al., 2012, ApJ, 750, L19
Sauer D. N. et al., 2008a, MNRAS, 391, 1605
Sauer D. N., et al., 2008b, MNRAS, 391, 1605
Schlegel D. J., Finkbeiner D. P., Davis M., 1998, ApJ, 500, 525
Shappee B. J., Stanek K. Z., 2011, ApJ, 733, 124
Steele I. A., et al., 2004, in SPIE Conference Series, Oschmann Jr. J. M., ed., Vol. 5489, SPIE, Bellingham WA, p. 679
Stehle M., Mazzali P. A., Benetti S., Hillebrandt W., 2005, MNRAS, 360, 1231
Stoll R., Shappee B., Stanek K. Z., 2011, ATEL 3588
Stritzinger M., Mazzali P. A., Sollerman J., Benetti S., 2006, A&A, 460, 793
Sullivan M., et al., 2011, ApJ, 737, 102
Suzuki N., et al., 2012, ApJ, 746, 85
Tanaka M., Mazzali P. A., Stanishev V., Maurer I., Kerzendorf W. E., Nomoto K., 2011, MNRAS, 410, 1725
Tanaka M., et al., 2008, ApJ, 677, 448
Timmes F. X., Brown E. F., Truran J. W., 2003, ApJ, 590, L83
Vinkó J., et al., 2012, A&A, 546, A12
Walker E., et al., 2012, MNRAS, 427, 103
Wang X., et al., 2012, ApJ, 749, 126
Yaron O., Gal-Yam A., 2012, PASP, 124, 668